Ph.D. Dissertation

Controllable Formation of Zero-twisted 2D Layers *via* Atomic Reconstruction

원자 재배열을 통한
제로 트위스트 2차원 물질의 제어 가능한 형성

August 2023

Graduate School of Engineering
Seoul National University
Material Science and Engineering Major

Ji-Hwan Baek

Controllable Formation of Zero-twisted 2D Layers *via* Atomic Reconstruction

Name of Examiner Gwan-Hyoung Lee

Submitting a Ph.D. Dissertation of Engineering

August 2023

Graduate School of Engineering
Seoul National University
Material Science and Engineering Major

Ji-Hwan Baek

Confirming the Ph.D. Dissertation written by
Ji-Hwan Baek
June 2023

Chair	Hyejin Jang	(Seal)
Vice Chair	Gwan-Hyoung Lee	(Seal)
Examiner	Myungjae Lee	(Seal)
Examiner	Chul-Ho Lee	(Seal)
Examiner	Jangyup Son	(Seal)

Abstract

Moiré superlattices in twisted van der Waals (vdW) layered structures have been studied widely to investigate unique and unprecedented electronic and optical phenomena. Despite perfectly zero-twisted bilayers are most energetically stable, achieving perfect alignment of stacked 2D layers remains challenging due to the limitations of mechanical manipulators, resulting in the inevitable formation of incommensurate domain boundaries around the commensurate reconstructed domains. This study investigates the formation of fully commensurate (FC) structures in twisted transition metal dichalcogenide (TMD) bilayers through thermally induced atomic reconstruction. The research focuses on a novel method for achieving zero-twisted TMD layers by utilizing encapsulation annealing to induce atomic rearrangement, regardless of initial twist angles and lattice mismatches. The resulting FC structures exhibit perfectly aligned crystalline orientations and opposite strains in adjacent layers.

The study demonstrates the fabrication of FC structures in TMD homo- and hetero-bilayers using encapsulation annealing. This approach enables better control over interfacial properties and opens opportunities for fundamental studies and diverse applications. The optical properties of FC structures are also examined.

Investigating the effect of stacking types on FC structure formation in TMD hetero-bilayers reveals distinct mesoscopic and microscopic structures based on R-stack and H-stack configurations. This approach is validated to large lattice-mismatched hetero-bilayers, such as $MoS_2/MoSe_2$ and WS_2/WSe_2, which presents a challenge for achieving self-reconstruction and atomic alignment. The impact of lattice mismatch on the atomic rearrangement process is investigated, providing

insights into achieving FC structures in such systems. Moreover, I elucidate the atomic-scale mechanisms through in-situ scanning tunneling electron microscopy (STEM). Observations reveal sequential rotational ordering of crystal lattices, formation of nanoscale-aligned domains through atomic rearrangement, and the presence of defect pairs at moiré pattern boundaries. Furthermore, the improvement of ferroelectric properties in 3R-TMD bilayers, particularly in FC structures, is investigated. Structural homogeneity in FC structures enhances interfacial sliding ferroelectricity compared to near-zero stacked TMD bilayers with separated domains and topological defects.

Overall, this thesis advances the understanding of FC structure formation in TMD layers and its implications for novel physical phenomena and potential applications. The findings highlight the significance of thermally induced atomic reconstruction in achieving fully commensurate structures with controlled properties, paving the way for advancements in two-dimensional materials research.

Keyword : Atomic reconstruction, Twist angle, Encapsulation annealing, Stacking order, Sliding ferroelectricity,
Student Number : 2019-29791

Table of Contents

Chapter 1. Introduction

1. Introduction

Following the discovery of monolayer two-dimensional (2D) materials, such as graphene, transition metal dichalcogenides (TMDs), hexagonal boron nitride (hBN) (*1-3*), extensive research has been studied on the physical properties of pristine 2D materials and vertically stacked van der Waals (vdW) layered structures. As research on vdW heterostructures has progressed (*4-6*), it has been revealed that the spatial overlapping of 2D materials in vdW heterostructures can induce a modulation of interlayer coupling strength, resulting in unprecedented behaviors of charged particles (*7-10*). The observation of unconventional superconductivity and unprecedented insulating electronic states in magic angle twisted-bilayer graphene (TBG) (*11, 12*) has highlighted the importance of the twist angle between two constituent layers in vdW layered structures, as it determines their electronic and optical properties by generating quantum mechanically hybridized electronic states (*13-15*). Twisted vdW layered structures exhibit periodic moiré superlattices, which further modify the interlayer coupling strength and electronic band structures. These moiré superlattices contribute to the formation of correlated-insulating states by creating flat mini-bands and manifest optical signatures of moiré potential-trapped interlayer excitons (*16-23*). Consequently, twisted vdW layered structures have emerged as promising candidates for investigating novel physical phenomena with 2D materials.

In moiré superlattices, the presence of three high-symmetric points, which have different atomic configurations, results in a spatial variation of interfacial vdW energy (*17, 24, 25*). Recently, in marginally stacked 2D layers, it was reported that

the moiré superlattices can be reconstructed into energetically more stable structures to reduce total vdW energy and relax the strain, expanding energetically stable structures and shrinking unstable structures (*26-35*). This phenomenon is usually called a self-atomic-reconstruction (or self-reconstruction), a result of self-reconstruction in marginally twisted 2D layers, periodic domains of energetically stable commensurate structures can be formed and separated by unstable incommensurate boundaries. Despite perfectly zero-twisted bilayers are most energetically stable (*26*), achieving perfect alignment of stacked 2D layers remains challenging due to the limitations of mechanical manipulators, resulting in the inevitable formation of incommensurate domain boundaries around the commensurate reconstructed domains.

In this study, I propose a novel method for achieving fully commensurate (FC) 2D layers with a zero-twist angle. Our approach involves thermally inducing an atomic reconstruction of twisted 2D layers using encapsulation annealing, regardless of the initial twist angles and lattice mismatches. This process results in perfectly aligned crystalline orientations of H- or R-type structures across the entire stacked area, along with opposite strains in adjacent layers.

In **Chapter 2**, general backgrounds on the physical properties of TMDs and twisted vdW heterostructures are provided. It also discussed that experimental and theoretical approaches for self-reconstruction in near-zero stacked 2D layers.

In **Chapter 3**, a formation of FC structure of TMD homo- and hetero-bilayers *via* encapsulation annealing is demonstrated, enabling better control over interfacial properties for fundamental studies and various applications.

In **Chapter 4**, our approach for controlling stacking order of FC structures are discussed. I demonstrated that a stacking type of two TMDs, R- and H-stack,

determines the final atomic configuration of FC structures.

In **Chapter 5**, I further discussed the thermally induced atomic reconstruction in twisted TMD hetero-bilayers with large lattice mismatch. Due to large lattice mismatch, a microscopic atomic structure of reconstructed hetero-bilayers

In **Chapter 6**, I demonstrated atomic-scale mechanisms of thermally induced atomic reconstruction *via* in-situ scanning tunneling electron microscopy (STEM) by applying a sequence of short heat pulses.

In **Chapter 7**, an improvement of ferroelectric properties of 3R-TMDs is demonstrated, resulting from structural homogeneity of FC structures due to absence of incommensurate domains in FC structures unlike self-reconstructed TMD bilayers.

In Chapter 8, the work is summarized and concludes.

Chapter 2. Background

2.1. Transition Metal Dichalcogenides and their Hetero-structures

2.1.1. Transition Metal Dichalcogenides

Transition metal dichalcogenides (TMDs), denoted as MX_2 (M: transition metal & X: chalcogen), are a class of layered two-dimensional (2D) materials. Each individual monolayer forms a hexagonal quasi-2D lattice, similar to the structure of graphene, through covalent bonding between X, M, and X atoms (Fig. 1a), and individual TMD layers are coupled with vdW bonding (*36-38*). TMDs display a wide range of material properties, depending on the specific composition. For instance, NbS_2, $NbSe_2$, TaS_2, $TaSe_2$, T_d-$MoTe_2$, and T_d-WTe_2 exhibit semimetallic behavior (*39-44*), whereas MoS_2, WS_2, $MoSe_2$, WSe_2, ReS_2 and 2H-$MoTe_2$ behave as semiconductors (*6, 45-47*). In this study, I focused on the group-VIB semiconducting TMDs (MoS_2, $MoSe_2$, WS_2, and WSe_2). Monolayers of the group-VIB TMDs (1L-TMDs) are known as direct bandgap semiconductors where both of conduction and valence band edges are located at the corner of hexagonal Brillouin zone (BZ), denoted as *K* and -*K* points (Fig. 1b) (*48-53*). The electronic band structures of TMDs exhibit variation depending on the specific composition of constituent atoms within the material.

1L-TMDs exhibit two distinct properties: the absence of inversion symmetry and strong spin-orbit coupling (SOC) strength (*50-52*). The inversion symmetry breaking leads to break of the spin-degeneracy of conduction and valence bands. Subsequently, the strong SOC strength causes band splitting of each spin-states through the Zeeman effect. Owing to this unique electronic band structure, optical transitions in 1L-

TMDs can be determined by spin- and valley-dependent optical selection rule, facilitating the quantum manipulation of valley pseudospin. Furthermore, the reduced dielectric screening effect in 2D nature gives rise to strong Coulombic interactions between electrons and holes, resulting in the formation of excitons with significantly high binding energies in TMDs. Consequently, TMDs have been extensively explored in diverse research fields focusing on optical phenomena.

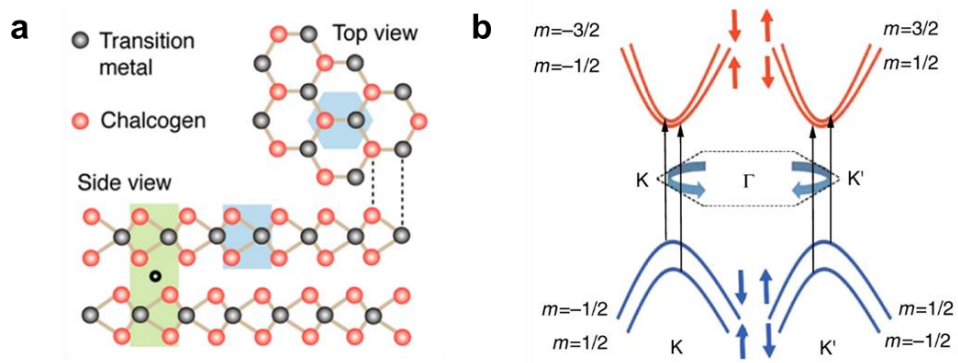

Figure 1. (a) Schematic of the atomic structure of TMDs. (*36*) (b) Schematic of electronic band structures of monolayer TMDs around K and - K points representing spin-orbit coupling-induced band splitting (*53*).

2.1.2 van der Waals Heterostructures of Transition Metal Dichalcogenides

The van der Waals (vdW) layered structure of 2D materials offers an advantage in the fabrication of heterostructures by stacking different 2D materials, independent of lattice mismatch (*4, 46*). Due to that versatility of vdW heterostructures, it has been widely studied on vdW heterostructures with various combinations of 2D materials (*54-58*). Given the diverse electronic band structures of TMDs arising from their different chemical compositions, stacking two layers of different TMDs allows for the formation of semiconductor/semiconductor junctions with distinct band alignments. In particular, when two TMDs are stacked to achieve a staggered type-II band alignment, interlayer coupling in the heterostructures facilitates spontaneous interlayer charge transfer, resulting in preferential localization of electrons and holes within energetically more stable layers (*14, 17, 33, 59-62*). Although electrons and holes are separated in type-II heterostructures, the remarkable strong exciton binding energy in TMDs enables the formation of spatially indirect excitons with separated electrons and holes, referred to as interlayer excitons. The emergence of interlayer excitons in TMD heterostructures highlights their exceptional potential as a versatile platform for exploring and unraveling novel realms of exciton physics.

2.2. Twist Angle in van der Waals Heterostructure

In artificially stacked vdW heterostructures, periodic moiré superlattices can be formed when the crystalline orientation between constituent layers is twisted (Fig. 2a) (*63*). The difference of crystalline orientation is called a twist angle (θ). A long-range three-fold rotation symmetry exhibits in moiré superlattices and exhibits varying periodicity depending on the twist angle. The modulation of electronic band structures in twisted 2D layers and the interlayer hybridization of electronic wavefunctions are attributed to this additional long-range symmetry. Consequently, the electrical and optical properties of twisted 2D bilayers can be controlled by manipulating the twist angle.

Notably, when two layers of graphene are stacked at specific small angle, it has been revealed that unconventional insulating electronic states and superconductivity can be achieved from twisted bilayer graphene (TBG) (Fig. 2b-c) (*11*). In twisted TMD heterostructures, the 1st BZ of each TMDs is mismatched in the momentum space as the crystalline orientation of two TMDs is twisted in the real space (Fig. 2d) (*16, 17, 63*). This momentum mismatch in the 1st BZ results in the electronic band edges of TMDs becoming momentum-indirect, leading to the suppression of radiative recombination of interlayer excitons (Fig. 2e). Thus, the twist angle of moiré superlattices emerges as a novel degree of freedom for engineering the behavior of twisted 2D layers, allowing for the exploration of unprecedented physical phenomena.

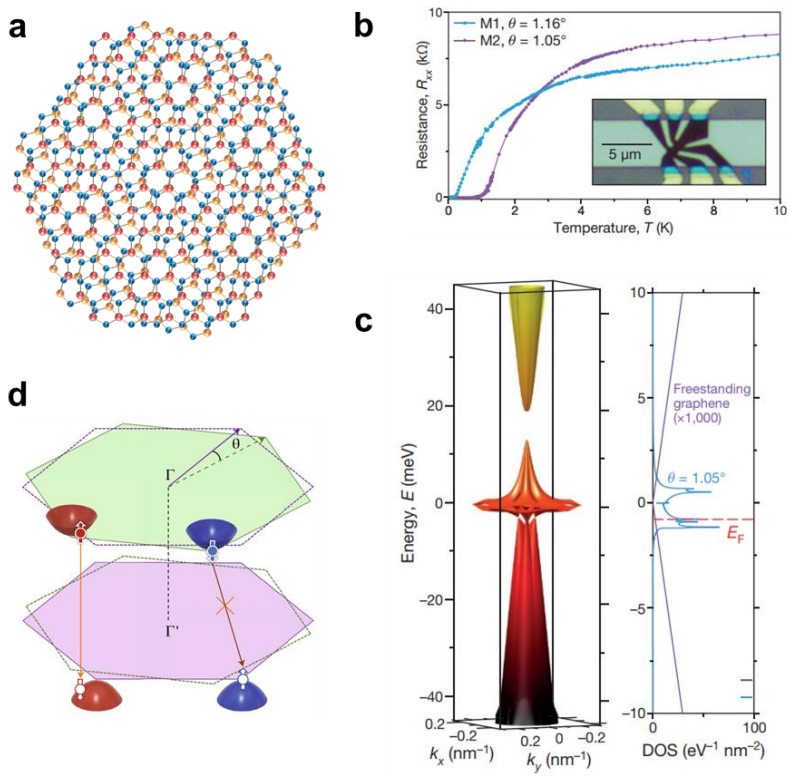

Figure 2. (a) Schematic of atomic structures of moiré superlattices in twisted 2D layers atomic structure of TMDs. (b) Superconductivity in magic-angle TBG (*11*). (c) Renormalized electronic band structure and density of states of magic-angle TBG. (*11*). (d) Schematic of electronic band structures of twisted TMD bilayers at momentum space (*16*).

2.3. Self-reconstruction in Near-zero-twisted Two-dimensional Layers

Twisted 2D layers exhibit the presence of three distinct high-symmetry points. In the case of twisted bilayer graphene (TBG), for instance, moiré superlattices display AB, BA, and AA stacking configurations, (Fig. 3a) (*27, 30, 34*). Since the interfacial energy of the van der Waals (vdW) interface depends on the atomic structure at the interface, variations in atomic configurations give rise to differences in interfacial energy (*26, 32*). In AA stacking, the atoms in the top and bottom layers align precisely in space, resulting in stronger electric repulsion compared to AB and BA stacking. To minimize the total energy, the energetically stable areas of AB and BA stacking expand, while the area of AA stacking contracts. Consequently, the atomic structure of TBG undergoes a spontaneous reconstruction, forming periodic domains of AB and BA stacking surrounded by saddle points (SP) and AA stacking (Fig. 3b). This spontaneous atomic reconstruction is commonly observed in twisted 2D layers with other 2D materials, such as TMD) and twisted hBN (*28, 33, 36, 37, 64*). The SP and AA structures represent topological defects that cannot be eliminated through continuous deformation, posing a significant challenge in achieving ideal zero-twisted 2D layers. Although the two layers are stacked in close proximity to 0˚, the formation of a periodic reconstructed structure is unavoidable due to the inherent inaccuracies in mechanical manipulation. Consequently, the fabrication of perfectly zero-twisted 2D layers remains an immensely challenging task.

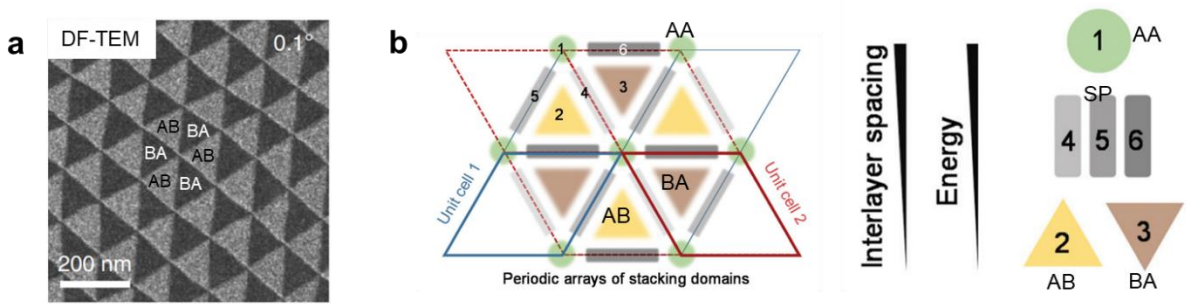

Figure 3. (a) Dark-field transmission electron microscopy (DF-TEM) image of self-reconstructed twisted bilayer graphene (TBG) (θ = 0.1˚) (*27*). (b) Schematic of mesoscopic structures of the self-reconstructed TBG (*32*). Interlayer spacing and interfacial vdW energy are varied with the atomic configuration.

Chapter 3. Formation of Zero-twisted Two-dimensional Layers *via* Thermally Induced Atomic Reconstruction

3.1. Introduction

As aforementioned in **Chapter 2.3**, it is difficult to fabricate perfectly zero-twisted 2D layers due to experimental limitation and inevitable formation of incommensurate topological defects, such as SP and AA domains. Here, we develop a novel approach to fabricate zero-twisted TMD layers by inducing atomic reconstruction in randomly stacked TMD layers. When twisted TMD layers are encapsulated with graphene (Gr) or hexagonal boron nitride (hBN) and annealed at high temperature (> 800˚C), I verified that crystalline orientation of TMD layers is aligned, I verified that twisted TMDs layers converted into the zero-twisted and lattice-matched FC structures regardless of initial twist angles (θ) and layer numbers. The reconstructed TMD layers exhibit commensurate structures inhomogeneously for whole overlapped regions of TMDs. Owing to their homogeneous and commensurate structure, I call zero-twisted TMD layers a fully commensurate (FC) structure. To evaluate the twist angle of twisted TMD layers and formation of FC structures, I used low-frequency (LF) Raman spectroscopy and photoluminescence (PL) measurements for interlayer excitons which are highly sensitive to the twist angle (*31, 61, 65-67*). Notably, the formation of FC structure is not attributed to a rotation of entire flakes but a local atomic rearrangement in whole overlapped regions *via* defect migration. The mechanism of thermally induced atomic reconstruction is discussed in **Chapter 6**. In this chapter, I will discuss the formation of FC structures and optical properties of FC structures of $WSe_2/MoSe_2$ hetero-

bilayers.

3.2. Methods

Sample preparation.

Flakes of hBN, Gr were first mechanically exfoliated from bulk crystals onto silicon substrates with 285 nm silicon oxide layer. Monolayer WSe_2 and $MoSe_2$ were either mechanically exfoliated from bulk crystals (from HQ Graphene). The thickness of monolayer WSe_2 and $MoSe_2$ were identified by optical contrast, photoluminescence (PL) measurements, and atomic force microscopy. Next, hBN/WSe_2/$MoSe_2$/hBN heterostructures for PL measurements were assembled with polycarbonate(PC)/ polydimethylsiloxane (PDMS) by dry-transfer method (*68*), and the pick-up temperatures for hBN and TMDs was around 115 ˚C and 75 ˚C. After stacking, heterostructures were transferred onto a clean SiO_2/Si substrate by releasing the PC film from the PDMS lens at a temperature above 180 ˚C. Finally, transferred samples were placed in chloroform for 3 h to remove the PC film covering heterostructures. Similar to hBN-encapsulated TMD bilayers, Gr-encapsulated TMD bilayers for TEM and STEM imaging were fabricated by dry-transfer method. To prevent the degradation of heterostructures during annealing, bi- or tri-layer graphene was used (*69*). However, since it is difficult to detach the Gr from the SiO_2/Si substrate due to stronger adhesion force between Gr/SiO_x rather than hBN/SiO_x (*70*), hBN is used as a top layer to easily detach the graphene. Thus, hBN/Gr/TMDs/Gr heterostructures were fabricated at first. Next, a XeF_2 gas, which can selectively etch only the hBN remaining the Gr (*71*), was treated on the heterostructures to remove the top hBN. To induce the atomic reconstruction in the twisted TMD layers, encapsulated TMD layers were annealed over 800˚C for 3 h in a vacuum of 10^{-4} Torr. Annealing temperature is varied with combination of

constituent TMDs: 800˚C for $WSe_2/MoSe_2$ and $MoSe_2/MoSe_2$, 900˚C for MoS_2/MoS_2 and WSe_2/WSe_2. The raising time of furnace temperature was 1 h and the furnace was naturally cooled to room temperature.

Transmission electron microscopy

TEM samples were prepared by using a poly (methyl methacrylate) (PMMA)-based wet transfer method. Samples on PMMA film were transferred on Si_3N_4 TEM grids (TEM windows, SN100-A20MP2Q05). The PMMA film was removed by placing samples in acetone for 24 h. HAADF-STEM images and SAED patterns were acquired Cs-corrected-monochromated TEM/STEM (Themis Z) at an operating voltage of 80 kV with a probe current of 30 pA, a 25 mrad convergence angle, and a collection angle range of 84-200 mrad.

Raman and PL spectroscopy

Low-frequency Raman spectra were acquired using Raman spectroscopy (Horiba LabRAM HR Evolution) with a 532 nm laser and a spot size of ~ 1 μm. PL spectra were acquired using Raman spectroscopy (JASCO) with a 532 nm laser and a spot size of ~ 1 μm. Micro-PL measurements at 77 K were conducted with a diode-pumped solid-state (DPSS) laser with the wavelength of 532 nm (2.33 eV) and the power of ~100 μW. A 40 × objective lens (N.A. = 0.6) was used to focus the laser on the samples with a spot of ~1 μm in diameter and to collect the PL signals from the samples. A substrate with exfoliated samples was loaded into an optical cryostat (Oxford MicrostatHe2) and cooled down to 10 K with liquid nitrogen and helium. The PL signals from the samples were dispersed with a Horiba TRIAX 320 spectrometer (300 grooves/mm) and was detected with a CCD using liquid nitrogen for cooling. The Raman and PL spectra were obtained at the same position before and after annealing.

3.3. Results and Discussion

Optical characteristics of $WSe_2/MoSe_2$ hetero-bilayer after encapsulation annealing

I fabricated a hBN-encapsulated $WSe_2/MoSe_2$ hetero-bilayer (θ = 6˚) (Fig. 4a), and annealed it by increasing annealing temperature from 400˚C to 1000˚C. Upon annealing at 800˚C, the emergence of PL emissions from interlayer excitons (X_I) in the $WSe_2/MoSe_2$ hetero-bilayer (Fig. 4b) was observed, whereas no X_I emissions were detected until annealing at 600˚C. The radiative recombination of interlayer excitons is prohibited by a momentum-dependent optical selection rule when the twist angle of hetero-bilayers deviated from 0˚ or 60˚, as the conduction and valence band edges of the two TMDs become momentum-indirect in reciprocal space (*61, 72*). In addition, an interlayer shear Raman mode (SM), which indicates the zero-twist-angle and strong interlayer coupling (*29*), emerged after encapsulation annealing after 800˚C (Fig. 4c). Thus, the emergence of X_I PL peaks and SM Raman peak suggests that crystalline orientations of WSe_2 and $MoSe_2$ are aligned after annealing at 800˚C. To verify the dependence of the twist angle on the emergence of X_I PL peaks, I investigated the PL emissions of $WSe_2/MoSe_2$ with different twist angles (θ = 59.7˚ and 45.5˚) before and after annealing. Although I cannot observe any change after annealing in optical images of hetero-bilayers (Fig. 5a-d), X_I PL peaks exhibit strong enhancement after annealing regardless of the twist angle (Fig. 5e-f). Moreover, the PL mapping images demonstrated that strong enhancement of X_I peaks was observed from entire overlapped regions of WSe_2 and $MoSe_2$ (Fig. 5g-h). Thus, the alignment of crystalline orientation of WSe_2 and $MoSe_2$ *via* encapsulation annealing can be generally achieved in

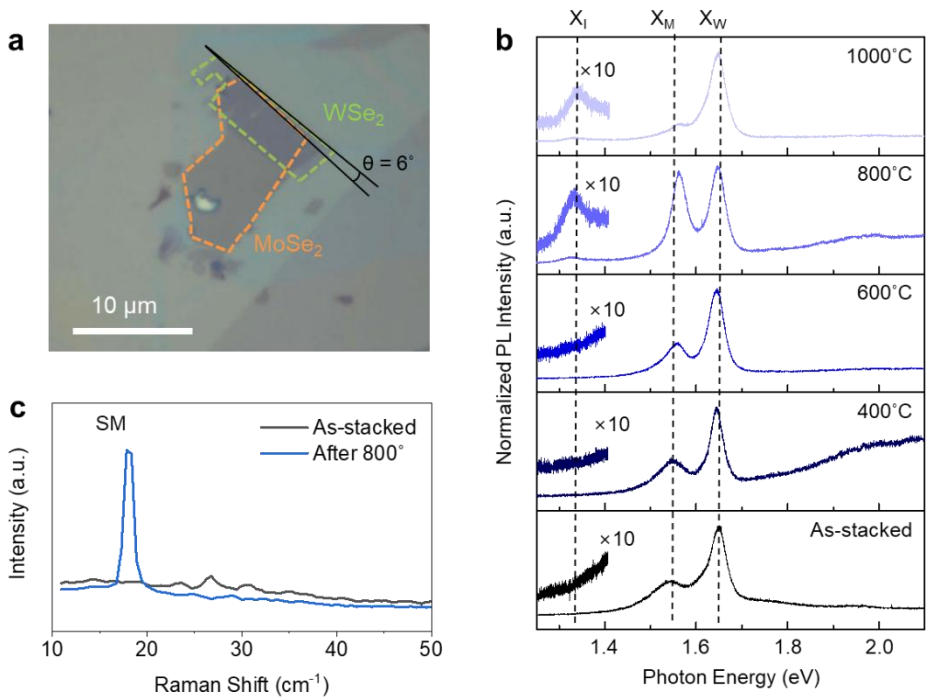

Figure 4. (a) Optical image of the randomly stacked $WSe_2/MoSe_2$ hetero-bilayer (θ = 6˚). Dash lines represent the monolayer flakes of WSe_2 and $MoSe_2$. (b) PL spectra of $WSe_2/MoSe_2$ by increasing annealing temperature**.** PL spectra of the hetero-bilayers obtained from the same sample before annealing, after annealing at 400˚C, 600˚C, 800˚C, and 1000˚C successively. The excitonic peak position is marked with black dash lines. Interlayer exciton emission peaks (X_I) were emerged after annealing at 800˚C. Intralayer excitons emissions peaks from $MoSe_2$ (X_M) and WSe_2 (X_W) show blueshift and redshift respectively after annealing.

randomly stacked $WSe_2/MoSe_2$ hetero-bilayers regardless of the initial twist angle. Figs. 6a and 6b displays the PL characteristics of interlayer exciton in $WSe_2/MoSe_2$ hetero-bilayers at 77 K with various twist angle before and after encapsulation annealing. While as-stacked HBLs exhibit different PL features by their twist angle (Fig. 6a), H-type FC show identical PL features despite of the different twist angle (Fig. 6b). The two distinct peaks were observed in H-type FC, and they identified as spin-singlet interlayer exciton (IX_S) and spin-triplet interlayer exciton (IX_T) (*73, 74*). Details for IX_S and IX_T are discussed below. To understand this difference in PL emissions, I analyzed the electronic band structure of hetero-bilayers before and after annealing. In as-stacked hetero-bilayers, a valence band maximum (VBM) of WSe_2 and conduction band minimum (CBM) of $MoSe_2$ deviated in the momentum space due to the lattice mismatch. Moreover, the long-range symmetry of moiré superlattices in as-stacked hetero-bilayers generates periodic potential which can induce the band renormalization of hetero-bilayers by interlayer hybridization of the wavefunction of two TMDs4,5,7-9,18 (*17, 18, 20-22, 33*). Therefore, interlayer excitons trapped in this moiré potential, generally called moiré excitons, contributed to different PL characteristics of as-stacked HBLs with different θ (Fig. 6c). Meanwhile, although the two FC $WSe_2/MoSe_2$ have different twist angle, they have same 2H atomic structures regardless of twist angle. Due to their identical atomic structure, they also have same electronic band structure, in which the VBM of WSe_2 and CBM of $MoSe_2$ are well-aligned at the *K* valley in momentum space as shown in Fig. 6d. Therefore, uniform PL characteristics can be obtained from H-type FC with different θ. Due to well-aligned band edges of WSe_2 and $MoSe_2$ with no momentum mismatch in H-type FC, interlayer exciton resides at the *K* (*-K*) valley in the momentum space. As-shown in Fig. 6b, the PL spectra of H-type FC show two

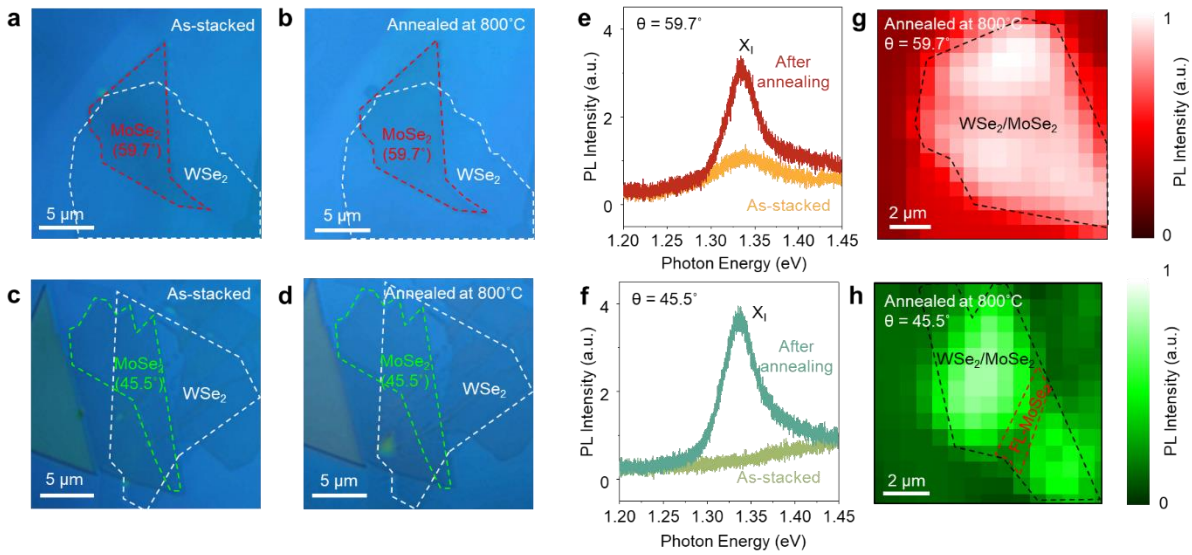

Figure 5. (a-d) Optical images of $WSe_2/MoSe_2$ as-stacked and after annealing with θ = 59.7˚ (a,b) and θ = 45.5˚ (c,d). (e-f) Interlayer excitons PL emissions in $WSe_2/MoSe_2$ before and after annealing with θ = 59.7 (e) and θ = 45.5˚(f). (g,h) Spatial mapping images of the integrated PL from 1.3 eV to 1.4 eV with θ = 59.7˚ (g) and θ = 45.5˚ (h). Dash lines represent the overlapped regions of $MoSe_2$ and WSe_2 flakes.

representative interlayer excitons emissions peaks, IX_S and IX_T, which were attributed to a splitting of CBM of $MoSe_2$ by strong spin-orbit coupling strength in TMDs (*73, 74*). Because a mirror symmetry in out-of-plane direction is broken in hetero-bilayers, IX_S can contribute to radiative recombination in HBLs, while spin-singlet excitons is considered to be spin-forbidden optically dark exciton in monolayer TMDs due to presence of out-of-plane mirror symmetry (*17, 73*). It was verified that the difference in PL peak position between IX_S and IX_T (24-25 meV) is consistent with the energy difference between up- and down-spin CBM of $MoSe_2$ (Δ_{CB}) (*74*). Moreover, the intensity ratio of IX_S and IX_T from different θ, corresponding to the theoretical value calculated from Boltzmann distribution of interlayer excitons (*73*). Thus, these PL measurements at 77 K imply that the H-stack hetero-bilayer is reconstructed to the ideal 2H atomic structure which has exactly zero-twist angle *via* encapsulation annealing.

Structural characterization of $WSe_2/MoSe_2$ after encapsulation annealing.

In order to provide further evidence that the emergence of X_I PL peaks is a result of structural reconstruction of the twisted hetero-bilayers into aligned structures, I measured a microscopic atomic structure of Gr-encapsulated $WSe_2/MoSe_2$ hetero-bilayers (θ = 46.9°) by using high-angle annular dark field scanning electron microscopy (HAADF-STEM) before and after annealing. The HAADF-STEM images in **Fig. 7** were obtained from the same position. As shown in low-magnification STEM images (Fig. 7a-b), no significant change was observed before and after annealing. However, after annealing the hetero-bilayer, I observed that the atomic structure of the hetero-bilayer transformed from twisted moiré superlattices into perfectly aligned 2H structures in entire regions of hetero-bilayer (Fig. 7c-d). I notated this aligned structure as a fully commensurate (FC) structure due to zero-

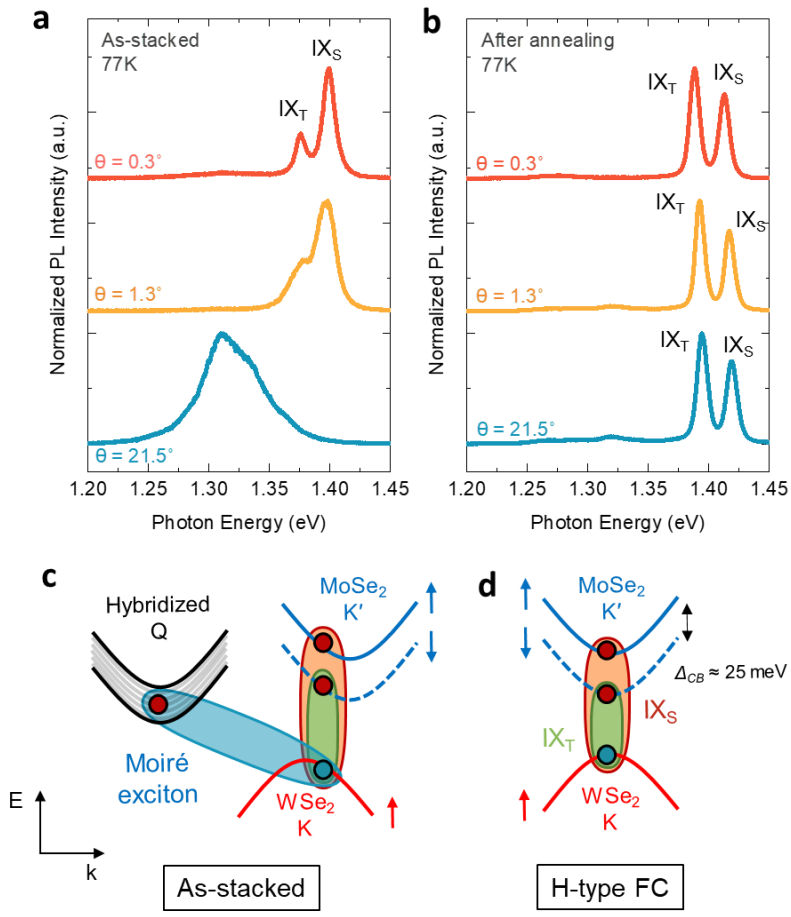

Figure 6. (a,b) PL spectra of $WSe_2/MoSe_2$ at 77 K with various twist angles before (a) and after annealing (b). (c,d) Schematic images of the electronic band structure of the incommensurate (c) and reconstructed (d) $WSe_2/MoSe_2$ hetero-bilayers. Circles represent electrons (red) and holes (jade). Solid (dash) lines represent the spin-up (down) bands.

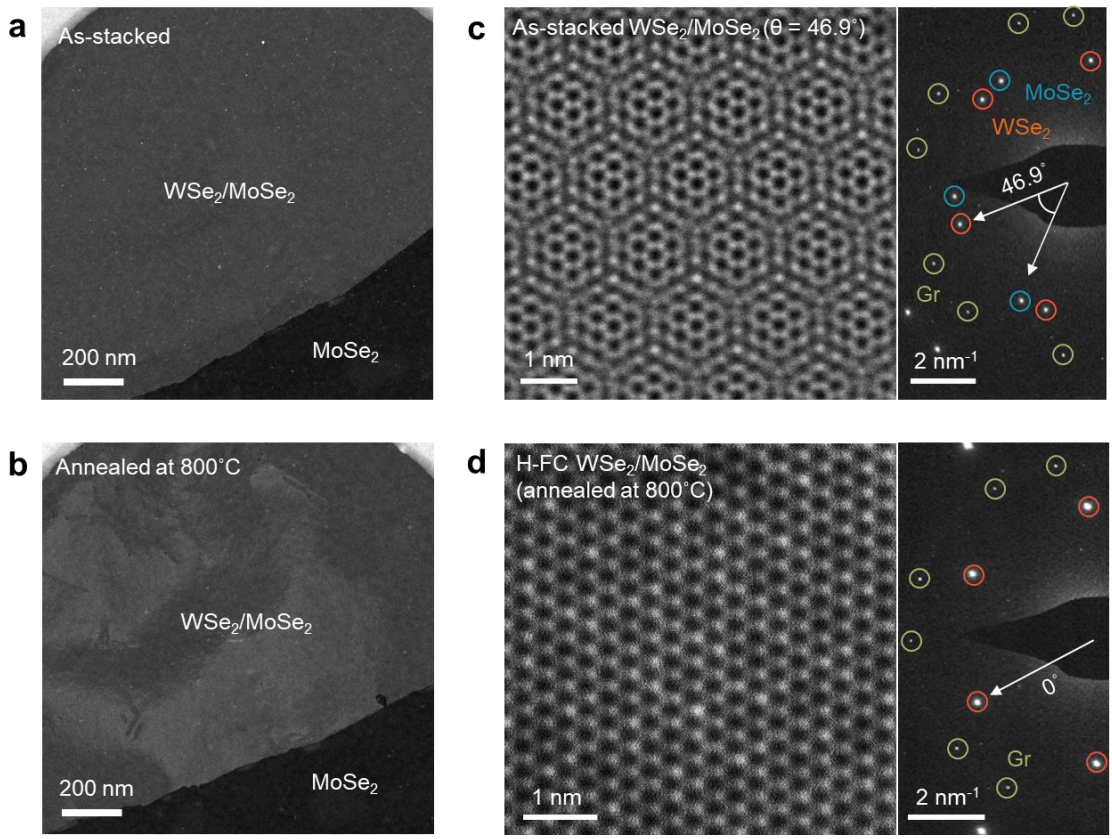

Figure 7. (a,b) Low-magnification HAADF-STEM images of the $WSe_2/MoSe_2$ hetero-bilayer (θ = 46.9°) as-stacked (a) and after annealing (b). (c,d) High-magnification HAADF-STEM images (left) with SAED images (right) of the $WSe_2/MoSe_2$ hetero-bilayer (θ = 46.9°) as-stacked (c) and after annealing (d).

twist-angle and zero-lattice-mismatch. These results are consistent with the emergence of X_I PL and SM Raman peaks after encapsulation annealing. As shown in selected area electron diffraction (SAED) images of the hetero-bilayer, the annealed hetero-bilayer exhibits alignment of WSe_2 and $MoSe_2$. By comparing a position of SAED peaks of TMDs with those of Gr before and after annealing, it can be confirmed that the $MoSe_2$ is aligned along the WSe_2. As shown in Fig.8, nanoscale boundaries were observed only in 1L- $MoSe_2$ regions after formation of FC structures whereas no boundaries in 1L-WSe_2 regions. These observations suggest that the thermal-induced atomic reconstruction in the stacked bilayers occurs through atom rearrangement within the weakly bonded layer, rather than the rotation of entire flakes. The reconstructed hetero-bilayer shows not only alignment of crystalline orientations of WSe_2 and $MoSe_2$ but also alignment of lattice constants of them despite of a lattice mismatch (δ) between WSe_2 and $MoSe_2$ (δ ~0.06%) (Fig. 9a). It implies that the WSe_2 which have relatively small lattice constant is expanded during atomic reconstruction, while the $MoSe_2$ is contracted. These lattice expansion and contraction were demonstrated by PL and Raman spectra of reconstructed $WSe_2/MoSe_2$ hetero-bilayers. As shown in PL spectra of $WSe_2/MoSe_2$ (Fig. 9b), PL emissions from intralayer excitons in $MoSe_2$ (X_M) exhibit blueshift after annealing, which indicates in-plane compressive strain is induced by the atomic reconstruction, while WSe_2 (X_W) shows redshift vice versa as a result of reconstruction-induced tensile strain. I observed same aspect of PL shifts of X_M and X_W in five different samples (Fig. 9c). Moreover, representative Raman peaks of $MoSe_2$ (A_{1g}) and WSe_2 (A′ and E′) also exhibit blue- and redshift, respectively. It is consistent with the PL shifts, indicating compressive and tensile strains are applied on $MoSe_2$ and WSe_2, respectively (Fig. 10).

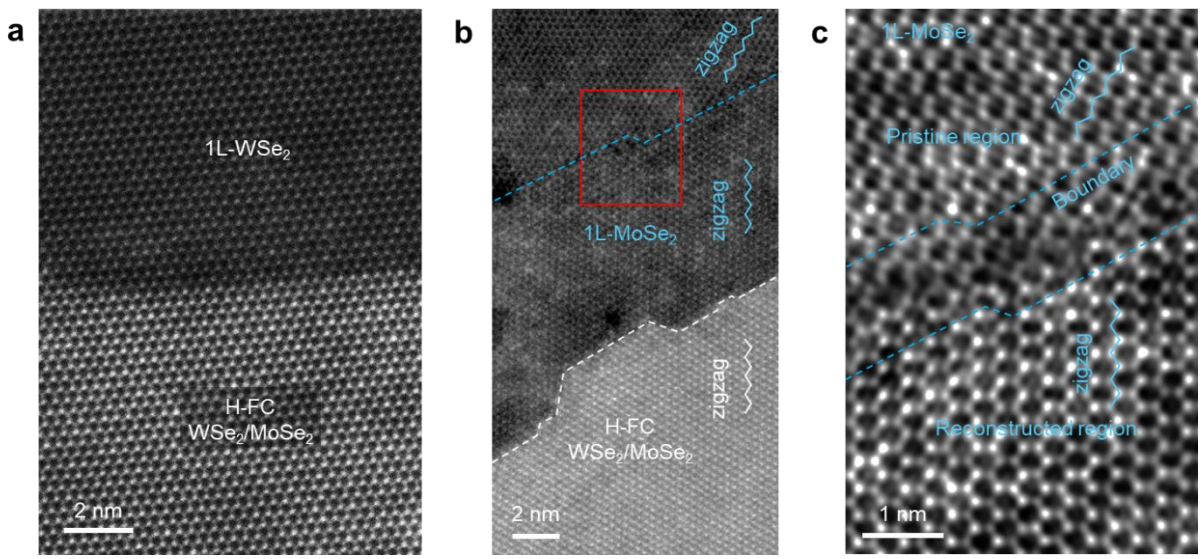

Figure 8. (a) HAADF-STEM images of partially overlapped regions of the $WSe_2/MoSe_2$ and 1L-WSe_2 after annealing. (b,c) HAADF-STEM images of partially overlapped regions of the $WSe_2/MoSe_2$ and 1L-WSe_2 after annealing. **c** is magnified image of the red box in **b**.

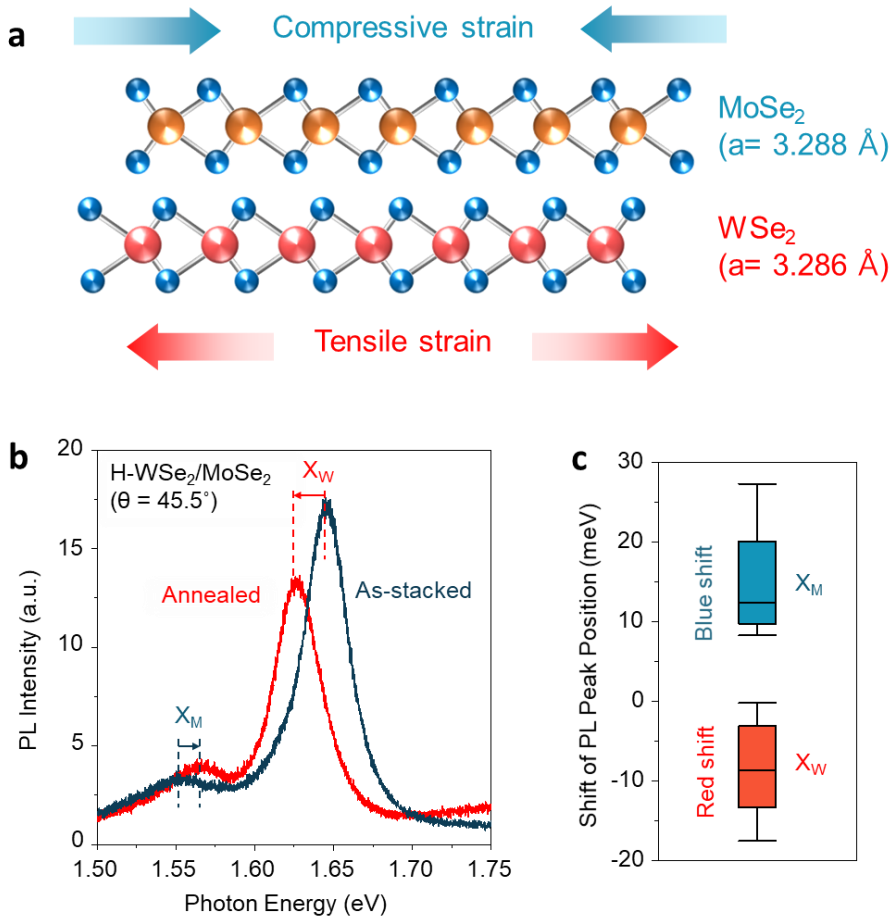

Figure 9. (a) A schematic of reconstruction-induced strain on the $WSe_2/MoSe_2$ hetero-bilayer. (b) Intralayer excitons PL spectra of $WSe_2/MoSe_2$ ($\theta = 45.5^{\circ}$) before and after annealing. (c) Shift of PL peak position of intralayer exciton of $MoSe_2$ (X_M) and WSe_2 (X_W) *via* encapsulation annealing.

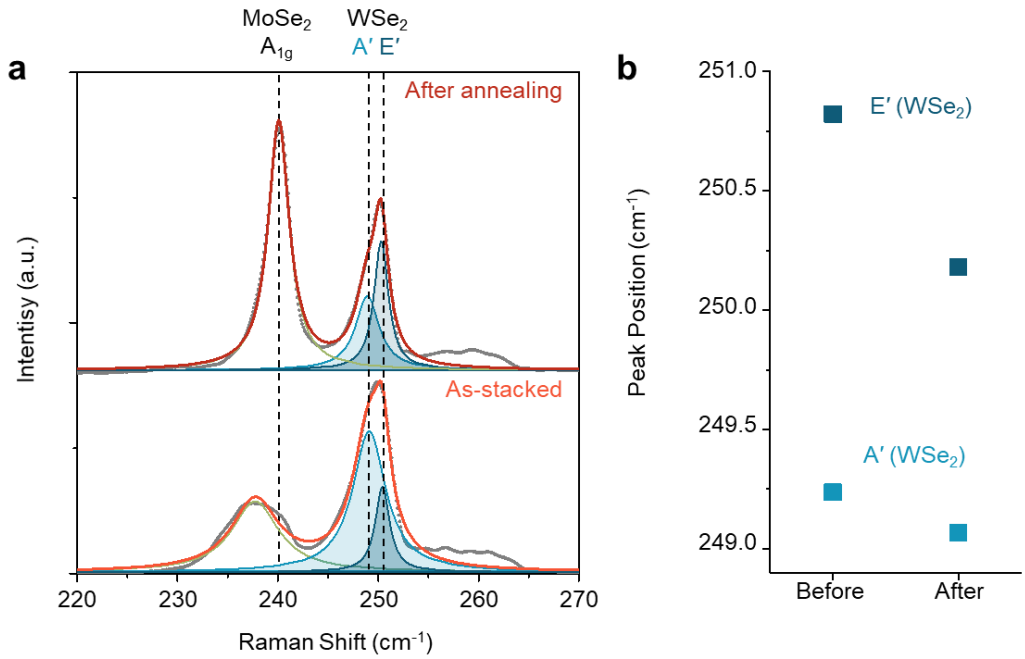

Figure 10. (a) Raman spectra of the $WSe_2/MoSe_2$ hetero-bilayer before and after annealing. (b) The difference of Raman peak position of WSe_2 before and after annealing.

Structural homogeneity of FC structures

Due to the presence of SP and AA stacking domains which cannot remove with spontaneous atomic reconstruction, a structure will spontaneously relax into periodic domains separated by strained domain walls by the self-reconstruction in near-zero stacked TMD bilayers. In contrast, thermally reconstructed hetero-bilayers do not exhibit such distinct domains as shown in low-magnification STEM images (Fig. 6b). To elaborately characterize the structural homogeneity of FC structures, I investigated dark-field TEM (DF-TEM) images from second diffraction planes of annealed $WSe_2/MoSe_2$ as shown in SAED images of Fig. 11a, $g_1 = (1\bar{2}10)$, $g_2 = (\bar{1}\bar{1}20)$, and $g_3 = (11\bar{2}0)$. The DF-TEM images reveal that there are no distinct domains with different optical contrast, which is in contrast to the as-stacked twisted $MoSe_2/MoSe_2$ bilayers where separated domains with different optical contrast (Figs. 11c-e). It indicates that FC structures are homogenous without separated domains. These DF-TEM observations provide further evidence of the homogeneity and coherence of the stacking order in FC structures on the larger scale.

Furthermore, I observed a decrease of full width half maximum of PL peaks of interlayer excitons in $WSe_2/MoSe_2$ hetero-bilayers after annealing. As shown in PL spectra at 77 K of $WSe_2/MoSe_2$ hetero-bilayers before and after annealing (Figs. 12a-b), I analyzed a linewidth of PL emissions of interlayer excitons in H-$WSe_2/MoSe_2$ with $\theta = 58.7^{\circ}$. The PL spectra were fitted with two peaks, corresponding to the IX_S and IX_T. The FWHM of the PL spectra was determined by using a Voigt function (*75*):

$$y = y_0 + A \cdot \frac{2ln2}{\pi^{3/2}} \frac{w_L}{w_G^2} \cdot \int_{-\infty}^{+\infty} \frac{e^{-t^2}}{(\sqrt{ln2}\frac{w_L}{w_G})^2 + (\sqrt{4ln2}\frac{x - x_c}{w_G} - t)^2} dt \qquad (1)$$

which is the convolution of the Gaussian and Lorentzian, where w_G and w_L are

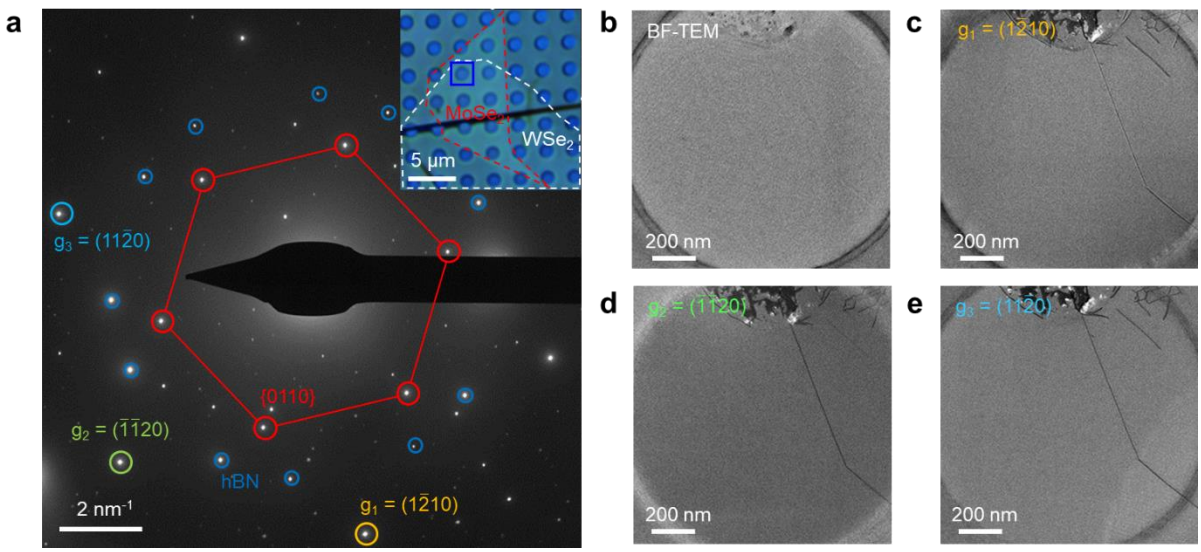

Figure 11. (a) SAED image of FC-WSe_2/$MoSe_2$ (θ = 59.7˚) after annealing at 800˚C. The inset shows the optical image of the sample. (b) Bright field TEM (BF-TEM) image of the FC-WSe_2/$MoSe_2$. (c-e) Dark field TEM (DF-TEM) images of the FC-WSe_2/$MoSe_2$ obtained from diffraction planes of g_1 = (1$\bar{2}$10) (c), g_2 = ($\bar{1}\bar{1}$20) (d), g_3 = (11$\bar{2}$0) (e) in **a**. All images were obtained from the blue box in the inset of **a**.

the FWHM of the Gaussian and Lorentzian components respectively, and A, y_0, and x_c are the area, baseline, and center of Voigt profile respectively. The FWHM of Voigt profile was approximated by eq. (2) (*76*).

$$w_V \approx 0.5346 w_L + \sqrt{0.2166 w_L^2 + w_G^2} \quad (2)$$

The PL peak position difference between IX_S and IX_T was measured as 24 meV both before and after annealing, which corresponds to the splitting energy of conduction band minimum of $MoSe_2$. Although the peak difference did not change after annealing, the FWHM of IX_S and IX_T decreased to 8.39 and 8.72 meV, respectively, approaching the thermal limit of kT (~ 6.64 meV at 77 K). In some samples, the linewidth further narrowed to 6.85 meV.

To investigate the thermal broadening of IX_S and IX_T, I measured PL spectra of FC-WSe_2/$MoSe_2$ at temperatures ranging from 10 K to 90 K. The FWHM of interlayer excitons was determined by fitting Lorentzian curves. As the temperature decreased from 90 K to 10 K, the PL linewidth decreased from 10.79 meV to 6.47 meV for IX_S and from 9.92 meV to 7.75 meV for IX_T (Figs. 13a-b). The temperature-dependent behavior of the PL linewidth was characterized by analyzing the FWHM (w) as a function of temperature (T) (Fig. 13c). The evolution of the PL linewidth of IX_S and IX_T was approximated using the following equation for phonon-induced broadening (*75*):

$$\mathrm{w} = w_0 + c_1 T + \frac{c_2}{e^{\Omega/k_B T} - 1} \quad (3)$$

where $w_0 = 7.58 \pm 0.14\, meV$ and $c_1 = 10.49 \pm 5\, \mu eV/K$ for IX_T and $w_0 = 5.82 \pm 0.35\, meV$ and $c_1 = 43.12 \pm 9\, \mu eV/K$ for IX_S. The parameter c_1 describes the linear increase in *w* caused by acoustic phonons, exhibits a similar magnitude as that reported in hBN-encapsulated 1L-MoS_2 ($w_0 = 4 \pm 0.2\, meV$ and

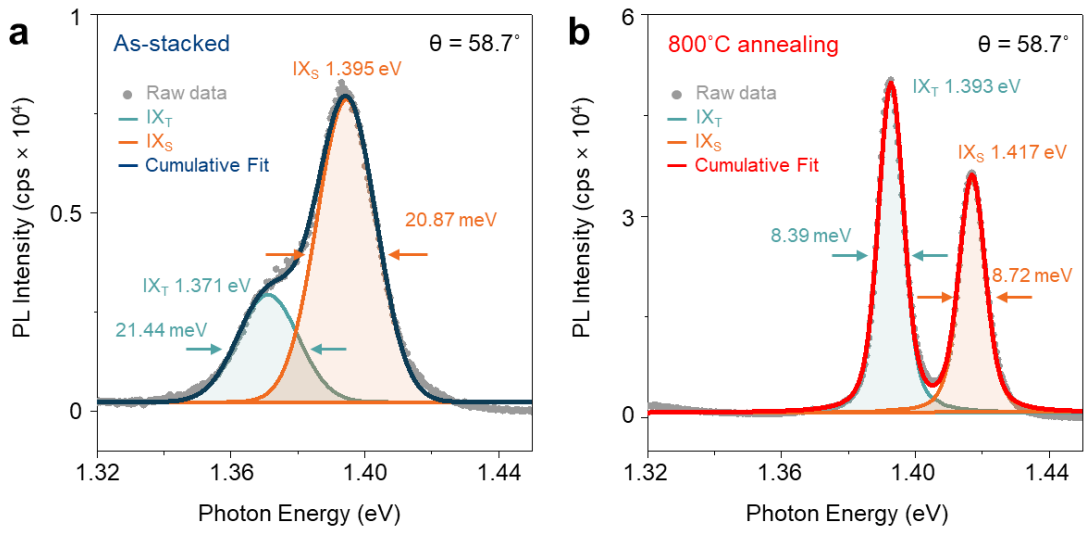

Figure 12. (a,b) Voigt-fitted PL spectra of spectral range of interlayer excitons in H-$WSe_2/MoSe_2$ ($\theta = 58.7^{\circ}$) as-stacked (a) and after annealing (b).

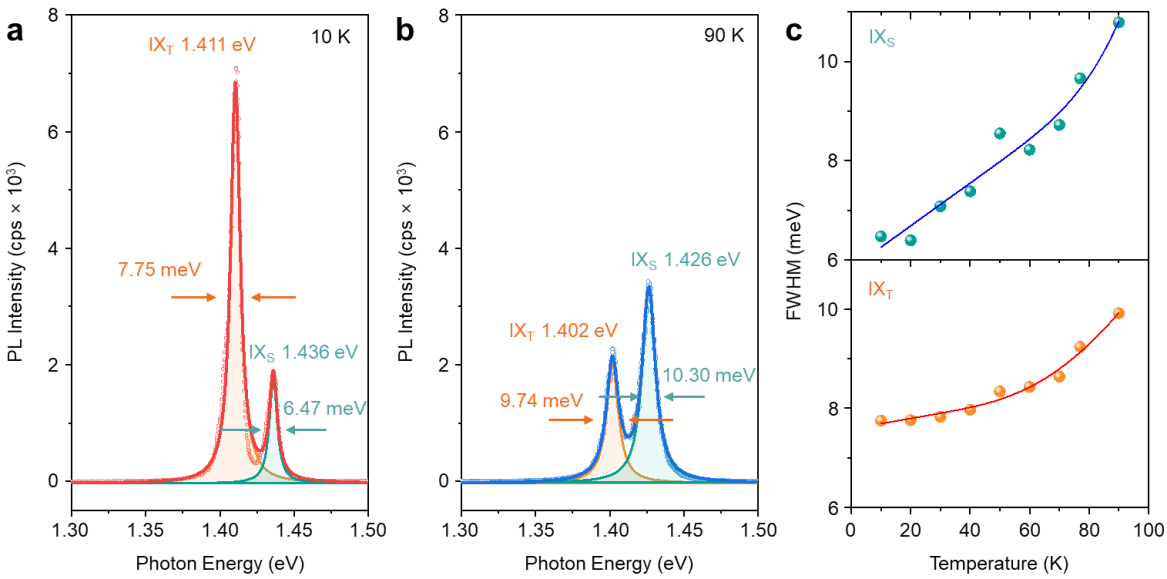

Figure 13. (a,b) Lorentzian-fitted PL spectra of spectral range of interlayer excitons in H-FC $WSe_2/MoSe_2$ measured at 10 K (a) and 90 K. (b). (c) FWHM of IX_S and IX_T as a function of temperature. Solid lines represent the fitted curve by equation (3).

$c_1 = 70 \pm 5\ \mu eV/K$) (*75*). It suggests that FC structures in our study exhibit a high degree of homogeneity. Furthermore, the parameter c_2, representing the strength of the phonon coupling, is determined to be 56.09 meV, while Ω, the averaged energy of the relevant phonons, is 28.81 meV. These values are also in the same order of magnitude as those reported for hBN-encapsulated MoS_2 (*75*). These result supports the structural homogeneity of the FC structures.

Atomic reconstruction in twisted TMD multilayers

To validate the achievement of thermally induced atomic reconstruction in twisted TMD multilayers, I investigated the layer-dependent Raman spectra of twisted multilayers of MoS_2 before and after annealing. LF and high-frequency (HF) Raman peaks were analyzed to understand the structural changes and interlayer interactions in the twisted MoS_2 multilayers. Moreover, I compared the Raman spectra of twisted homo-multilayers of MoS_2 with those of exfoliated-MoS_2, considering the well-established previous studies on the layer-dependent properties of Raman spectrum of MoS_2. As shown in Fig. 14a, the Raman spectra of exfoliated multilayer MoS_2 exhibited clear representative shear mode (SM) and layer breathing mode (LBM) peaks, consistent with previous reports. However, twisted MoS_2 homo-structures (θ = 55˚) did not display any interlayer Raman peaks before annealing, indicating weak interlayer coupling. Upon annealing at 900˚C, the stacked MoS_2 showed the emergence of SM and LBM peaks in LF regimes of Raman spectra similar to those observed in exfoliated MoS_2, indicating the formation of FC structures of MoS_2 multilayers after annealing. Furthermore, I observed the increase of peak difference between the $E_{2g}{}^1$ and A_{1g} peaks of MoS_2 with the number of layers

after annealing, compared with as-stacked MoS_2 multilayers (Figs. 14b-d). It is similar to the behavior typically observed in exfoliated MoS_2 multilayers, suggesting the crystalline orientations of each MoS_2 are aligned after annealing. In addition, I observed the formation of FC structures in a twisted WSe_2 trilayer after annealing at 950˚C as shown in the HAADF-STEM images (Fig. 15). Thus, I demonstrated that the thermally induced atomic reconstruction is validated for the multiply stacked TMD layers.

Effect of encapsulation of the atomic reconstruction of twisted TMD layers

To verify the effect of encapsulation on the thermally induced atomic reconstruction, I prepared a non-encapsulated $WSe_2/MoSe_2$ hetero-bilayer (θ = 54˚) as a control sample and annealed it with supplying Se flows to minimize a decomposition and evaporation of WSe_2 and $MoSe_2$. As shown in optical images of the hetero-bilayer after annealing under Se rich environment (Figs. 16a-c), it was confirmed that WSe_2 and $MoSe_2$ flakes were well maintained after annealing. After annealing under Se-rich environment, interlayer shear modes were not observed in LF regime of Raman spectra after annealing (Fig. 16d), which indicates the thermally induced atomic reconstruction did not occur without encapsulation despite of minimizing the decomposition of TMDs. Moreover, the full width half maximum (FWHM) of HF intralayer Raman peaks of $MoSe_2$ and WSe_2 increased after 900˚C (Fig. 16e), indicating a low crystallinity of non-encapsulated TMDs after annealing. Therefore, it is clear that the graphene or hBN encapsulation is essential to induce atomic reconstruction of twisted TMD layers.

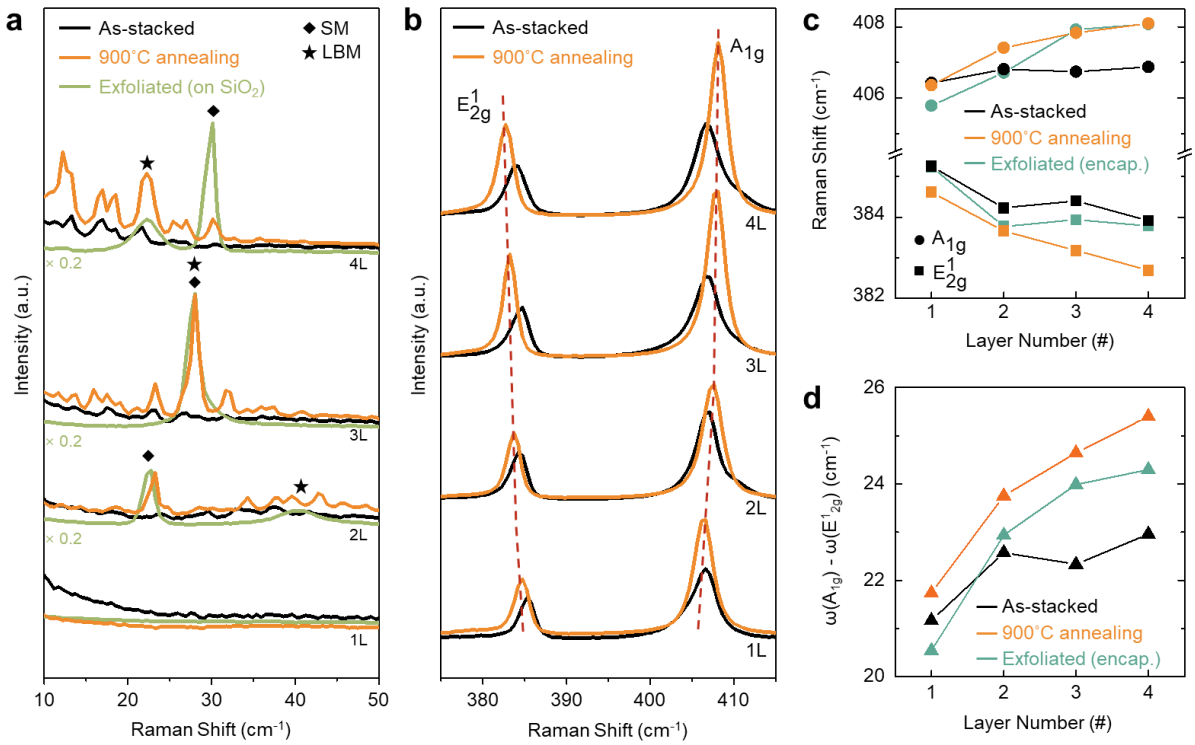

Figure 14. (a) Low-frequency Raman spectra of exfoliated MoS_2 (green), twisted as-stacked MoS_2 encapsulated with hBN (black), and after annealing stacked MoS_2 (orange). (b) High-frequency Raman spectra of twisted MoS_2 encapsulated with hBN (black), and after annealing them (orange). (c) Raman peak position of MoS_2 with various layer numbers. (d) Peak difference between E_{2g}^1 and A_{1g} as a function of layer numbers.

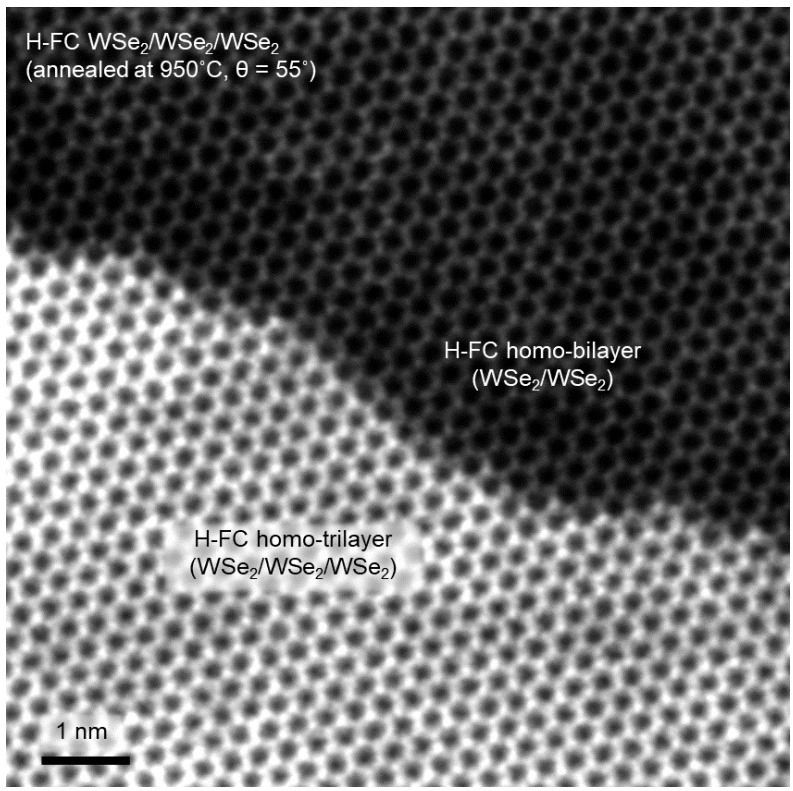

Figure 15. Atomic reconstruction in twisted WSe_2 homostructures. The HAADF-STEM image of WSe_2 homo-bilayer and homo-trilayer after annealing at 950˚C. The twist angle of each layer is 55˚.

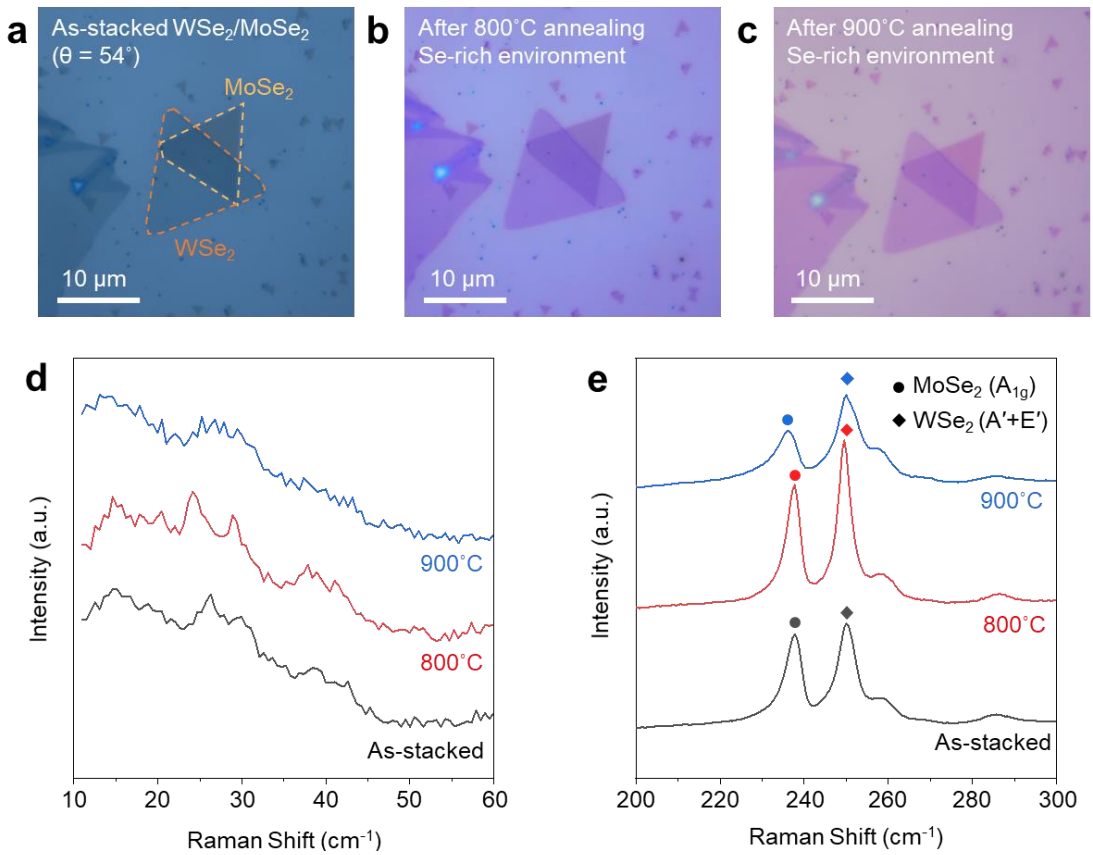

Figure 16. (a-c) Optical images of non-encapsulated $MoSe_2/WSe_2$ as-stacked (a) and after annealing at 800˚C (b) and 900˚C (c) under Se-rich environment. (d,e) Low-frequency (d) and high-frequency (e) Raman spectra of $MoSe_2/WSe_2$ before and after annealing under Se-rich environment.

3.4. Conclusion

In this chapter, I report the atomic reconstruction of randomly stacked TMD layers into FC structure, which only exists in theory and has not been realized thus far. The annealing process resulted in the emergence of PL emissions from interlayer excitons in the hetero-bilayer, indicating the alignment of crystalline orientations of WSe_2 and $MoSe_2$. The PL enhancements were observed regardless of the initial twist angle, suggesting that crystalline orientation alignment can be achieved in randomly stacked hetero-bilayers. Additionally, the structural characterization revealed that the atomic structure of the hetero-bilayer transformed from twisted moiré superlattices to perfectly aligned 2H structures after annealing. The reconstructed hetero-bilayer exhibited alignment not only in crystalline orientations but also in lattice constants, resulting in induced compressive and tensile strains in $MoSe_2$ and WSe_2, respectively. The homogeneity and coherence of the reconstructed structures were confirmed through microscopy techniques. The study also demonstrated the thermally induced atomic reconstruction in twisted TMD multilayers and highlighted the importance of encapsulation in achieving the desired structural changes. Overall, the findings contribute to the understanding of the optical and structural properties of hetero-bilayers and provide insights into the controlled manipulation of twisted TMD systems.

Chapter 4. Controlling Stacking Order of Fully Commensurate Structure

4.1. Introduction

I demonstrated the formation of zero-twisted and lattice-matched FC structure of TMD hetero-bilayers via encapsulation annealing in **Chapter 3**. As aforementioned in **Chapter 3**, marginally stacked TMD bilayers undergo self-atomic-reconstruction, forming periodic domains of commensurate structures to minimize the total van der Waals (vdW) interfacial energy. Previous studies have reported that the mesoscopic structures of self-reconstructed TMD bilayers vary depending on the stacking type of the TMDs (*29, 30, 33*). Specifically, when two TMD layers are stacked in parallel (nearly 0˚), they exhibit periodic triangular patterns upon reconstruction. Conversely, when the two TMD layers are stacked in anti-parallel (nearly 60˚), they undergo reconstruction, resulting in periodic hexagonal patterns. This observation applies not only to the mesoscopic structures but also to the microscopic structures of TMD bilayers: R-stack bilayers reconstruct to the 3R atomic configuration, while H-stack bilayers reconstruct to the 2H atomic configuration. In this chapter, I investigate the effect of the stacking type on the formation of FC structures using TMDs grown *via* chemical vapor deposition (CVD). However, the crystalline orientation of mechanically exfoliated TMDs cannot be controlled, resulting in a random distribution of zigzag and armchair configurations. Therefore, determining the stacking type of TMD bilayers requires structural characterization, such as second harmonic generation measurements and STEM measurements. In order to exert some control over the stacking type of twisted TMD

bilayers, I employed CVD-grown triangular TMD flakes, where the triangular edges correspond to a metal-zigzag edge (M-ZZ) (*77, 78*). This is based on the thermodynamic preference for M-ZZ edges during the growth process.

This chapter provides insights into the role of stacking type in modulating the formation of FC structures in twisted TMD bilayers. The control of stacking configurations paves the way for tailored material properties and device functionalities, propelling the field of two-dimensional (2D) materials toward exciting advancements.

4.2. Methods

Chemical vapor deposition growth

Monolayer crystals of WSe_2 and $MoSe_2$ were synthesized on SiO_2/Si substrates with SiO_2 thickness of 285 nm by chemical vapor deposition (CVD) with 2-inch quartz tube under ambient pressure. To synthesize monolayer WSe_2, a quartz boat with $WO_{2.9}$ powder (99.99%, Alfa Aesar) KI powder (99.99%, Alfa Aesar) was located at the center of the furnace and the SiO_2/Si substrate suspended face-down on top of the boat. Another quartz boat with selenium powder (99.99%, Sigma Aldrich) was located at the upstream of the quartz tube at a distance of 19.5 cm from the center of the furnace. The furnace temperature is raised up to 800˚C at a rate of 50˚C/min and maintained for 15 min and the furnace was naturally cooled to room temperature. 300 sccm of Ar were flowed for the whole growth process and 10 sccm of H_2 were flowed until the start of the cooling process. To synthesize monolayer $MoSe_2$, a quartz boat with MoO_3 powder (99.97%, Sigma Aldrich) was located at the center of the furnace and the SiO_2/Si substrate suspended face-down on top of the boat. Another quartz boat with selenium powder (99.99%, Sigma Aldrich) was located at the upstream of the quartz tube at a distance of 19.5 cm from the center of the furnace. The furnace temperature is raised up to 750˚C at a rate of 50˚C/min and maintained for 20 min and the furnace was naturally cooled to room temperature. 300 sccm of Ar were flowed for the whole growth process, and 10 sccm of H_2 was introduced from 20 minutes to 35 minutes after starting the growth process.

Transmission electron microscopy

TEM samples were prepared by using a poly (methyl methacrylate) (PMMA)-

based wet transfer method. Samples on PMMA film were transferred on Si_3N_4 TEM grids (TEM windows, SN100-A20MP2Q05). The PMMA film was removed by placing samples in acetone for 24 h. HAADF-STEM images and SAED patterns were acquired Cs-corrected-monochromated TEM/STEM (Themis Z) at an operating voltage of 80 kV with a probe current of 30 pA, a 25 mrad convergence angle, and a collection angle range of 84-200 mrad.

Raman and PL spectroscopy

Low-frequency Raman spectra were acquired using Raman spectroscopy (Horiba LabRAM HR Evolution) with a 532 nm laser and a spot size of ~ 1 μm. PL spectra were acquired using Raman spectroscopy (JASCO) with a 532 nm laser and a spot size of ~ 1 μm. The Raman and PL spectra were obtained at the same position before and after annealing.

4.3. Results and Discussion

Dependence of the stacking type on the atomic reconstruction

I fabricated Gr-encapsulated $WSe_2/MoSe_2$ hetero-bilayers by using CVD-grown TMD flakes with different stacking types: R- and H-stack (Fig. 17). Stacking types of TMD bilayers can be determined by how two triangular TMDs are aligned: R-stack at parallel alignment and H-stack at anti-parallel alignment (Fig. 18). In addition, I can fabricate R- and H-stack TMD bilayers in one sample simultaneously by using star-shaped polycrystalline 1L-TMDs, in which adjacent grains have opposite crystalline orientation. The HAADF-STEM images of Fig. 19 demonstrate that triangle edges of TMD flakes align in parallel with M-ZZ edges. Fig. 20 displays the HAADF-STEM images of nearly-zero (NZ) stacked $WSe_2/MoSe_2$ hetero-bilayers before and after annealing. Similar to previously reported results, periodic commensurate domains (3R for R-stack and 2H for H-stack) surrounded by incommensurate domains (SP and AA) were observed in as-stacked hetero-bilayers. However, annealed hetero-bilayers exhibit homogenous structures without any distinct domains and incommensurate regions unlike as-stacked hetero-bilayers (Figs. 21a-b). The atomic structure of reconstructed hetero-bilayers depends on the stacking type. R- (H-) stack hetero-bilayers reconstructed into FC structures with 3R (2H) configuration (Figs. 21c-d). I annotated FC structures which have 3R structure as "R-FC" and 2H as "H-FC". The selected-area electron diffraction patterns of $WSe_2/MoSe_2$ also indicate stacking-type-dependent atomic reconstruction of R- (H-) stack into R- (H-) FC. In NZ-stacked hetero-bilayers, two distinguishable SAED peaks were observed due to the presence of incommensurate

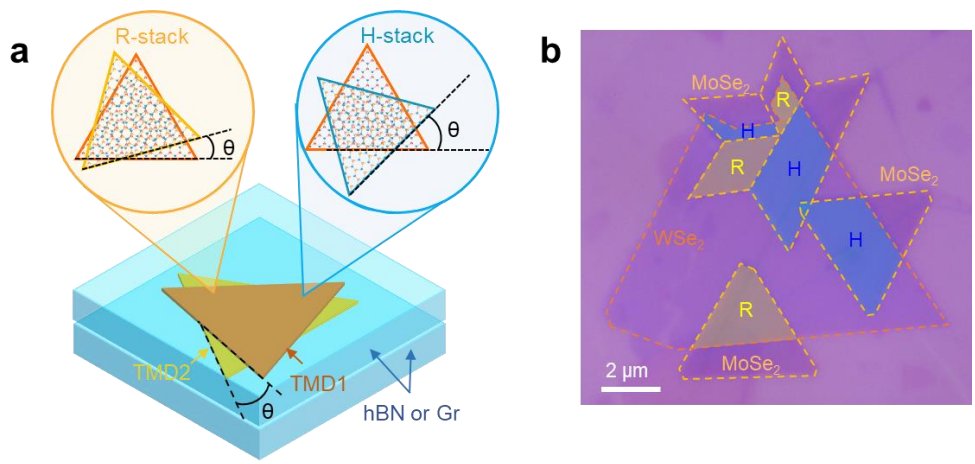

Figure 17. (a) Schematic images of twisted TMDs bilayers encapsulated by graphene or hBN with different stacking type (R- & H-stack). (b) Optical image of Gr/WSe_2/$MoSe_2$/Gr heterostructures with a different stacking type.

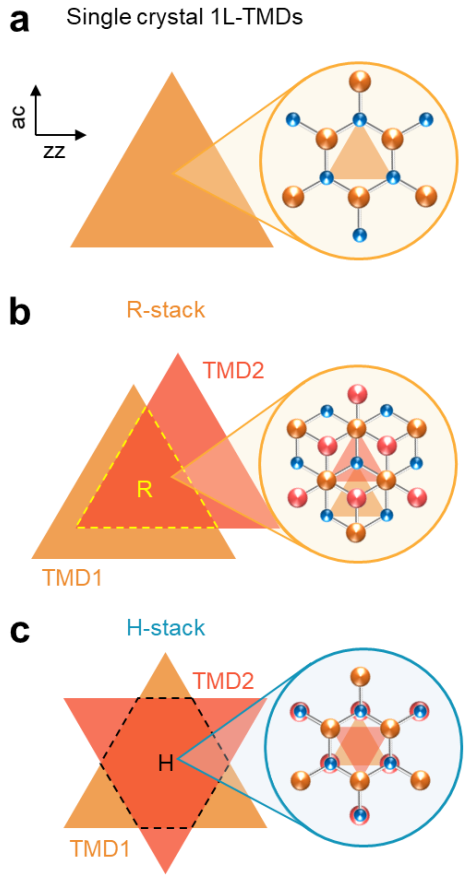

Figure 18. (a) Illustration of crystal structure of single crystal monolayer TMDs grown by CVD methods. Black arrows represent zigzag (zz) and armchair (ac) edges of TMDs. Circles represent metal (orange) and chalcogen (blue) atoms respectively. (b,c) Schematic of stacking type of TMDs bilayers. Two triangular TMDs are parallelly aligned in R-stack (b), while anti-parallelly aligned in H-stack (c).

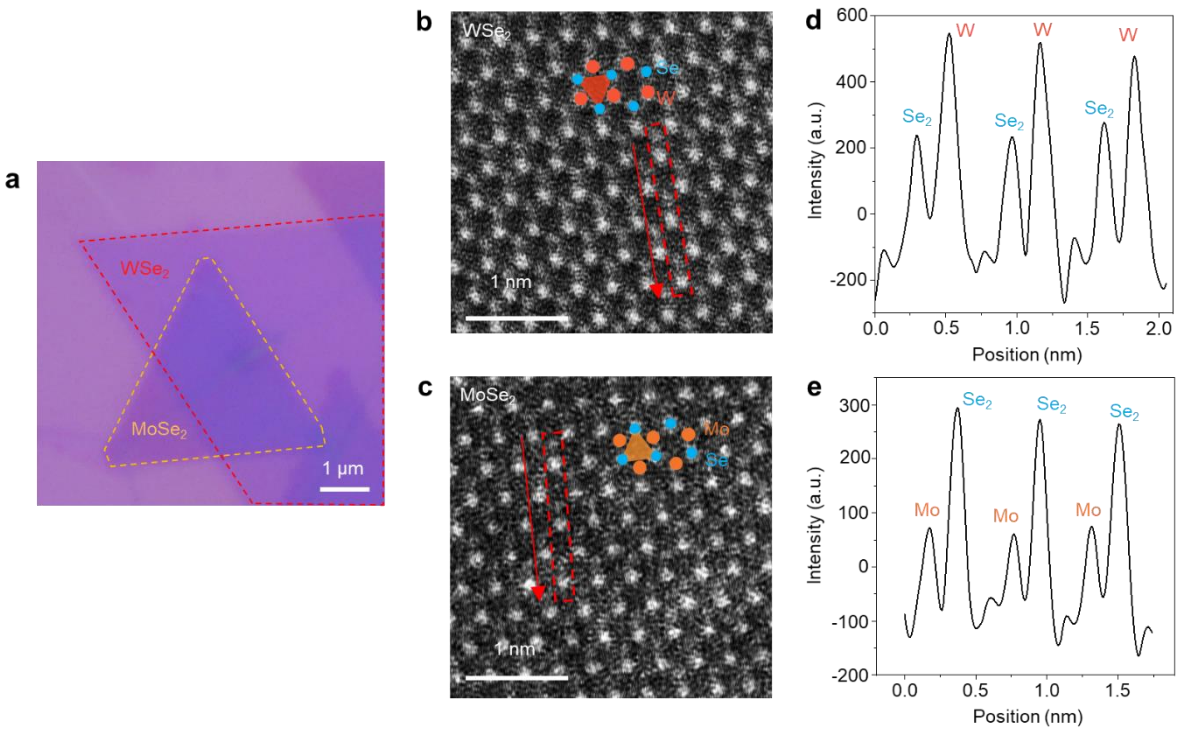

Figure 19. a, Optical image of H-stack $WSe_2/MoSe_2$ after annealing at 800˚C, which is the same sample depicted in Fig. 1b. (b,c) HAADF-STEM images of monolayer regions of WSe_2 (b) and $MoSe_2$ (c). Red, orange, and blue circles represent W, Mo, and Se atoms, respectively. (d,e) Intensity profiles of HAADF-STEM images of WSe_2 (d) and $MoSe_2$ (e) collected from red dash boxes in **b** and **c**.

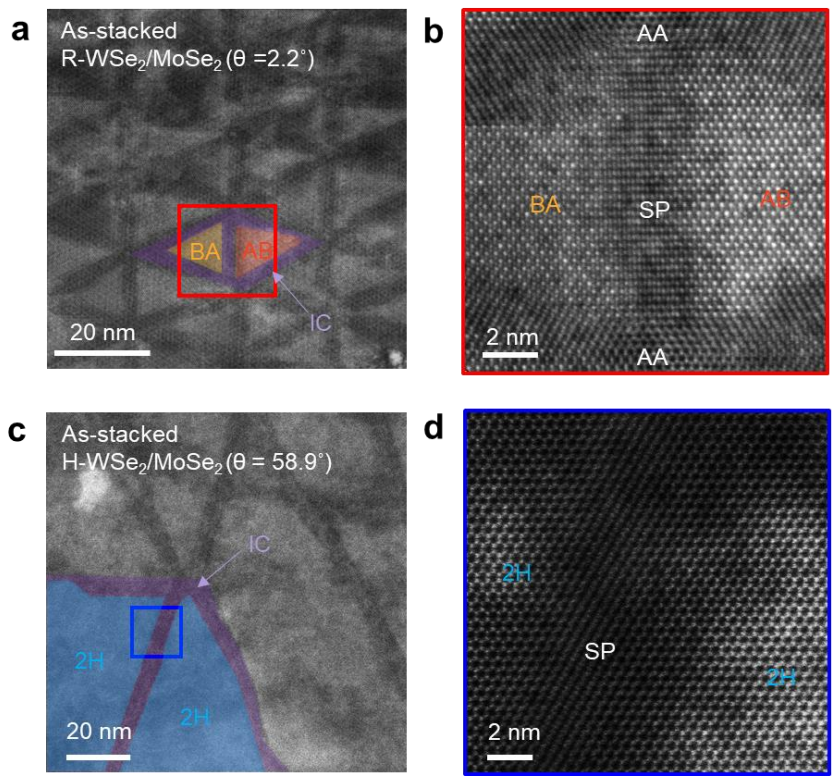

Figure 20. (a,b) HAADF-STEM images of the R-stack $WSe_2/MoSe_2$ hetero-bilayer ($\theta = 2.2^{\circ}$). False-colored regions in a represent AB (red), BA (yellow), and IC (purple) regions. (c,d) HAADF-STEM images of the H-stack $WSe_2/MoSe_2$ hetero-bilayer ($\theta = 58.9^{\circ}$). False-colored regions in a represent 2H (blue) and IC (purple) regions.

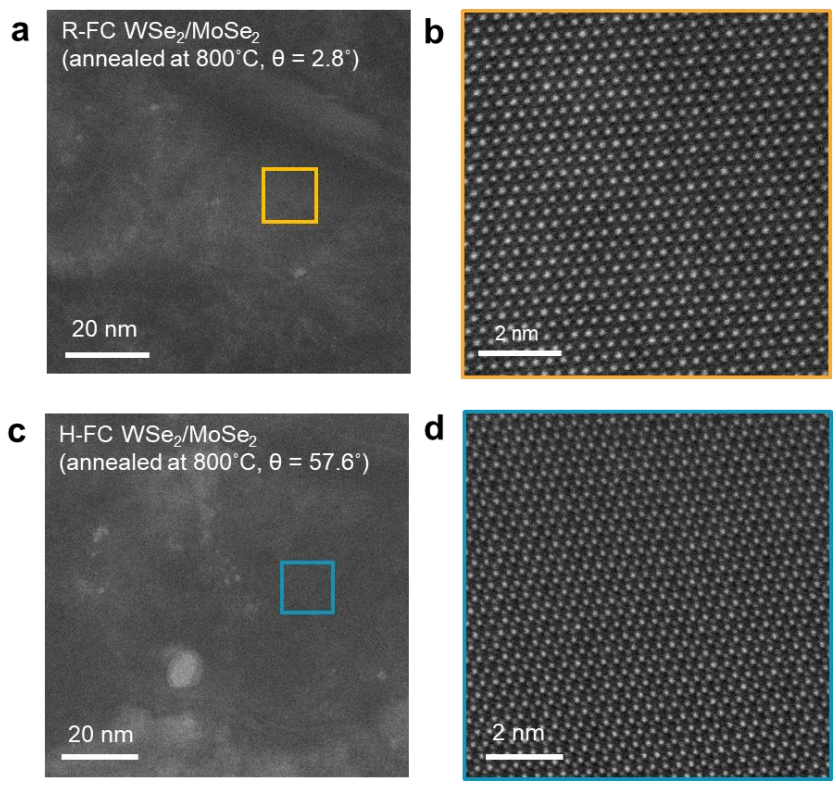

Figure 21. (a,b) HAADF-STEM images of the R-FC $WSe_2/MoSe_2$ hetero-bilayer (θ = 2.8˚) after annealing. (c,d) HAADF-STEM images of the H-FC $WSe_2/MoSe_2$ hetero-bilayer (θ = 57.6˚).

regions as a result of self-reconstruction (Fig. 22). In contrast, one sharp SAED peak was observed in FC-hetero-bilayers (Figs. 23a-d), indicating perfectly matched crystalline orientation and lattice constant of WSe_2 and $MoSe_2$. From the difference between average SAED intensity of {0110} and {1120} lattice planes (Fig. 23e), it can be also demonstrated the selective formation of R- and H-FC by controlling stacking type of hetero-bilayers.

The selective formation of R- and H-FC structures is also validated for the heterostructures of polycrystalline TMDs. I transferred the star-shaped polycrystalline $MoSe_2$, in which neighboring domains have opposite crystalline orientation, on the single crystal WSe_2 to investigate a stability of grain boundary during atomic reconstruction (Fig. 24a). As a result of encapsulation annealing, R- and H-stack regions reconstructed into R- and H-FC structures, respectively (Fig. 24b). 4|8 boundaries in $MoSe_2$ were well maintained after formation of FC structures (Fig. 24c), as a result, a seamless lateral junction of H- and R-FC was achieved in heterostructure of single crystal WSe_2 and poly-crystalline $MoSe_2$. It implies that 4|8 boundaries can migrate during atomic reconstruction without damage to atomic structure.

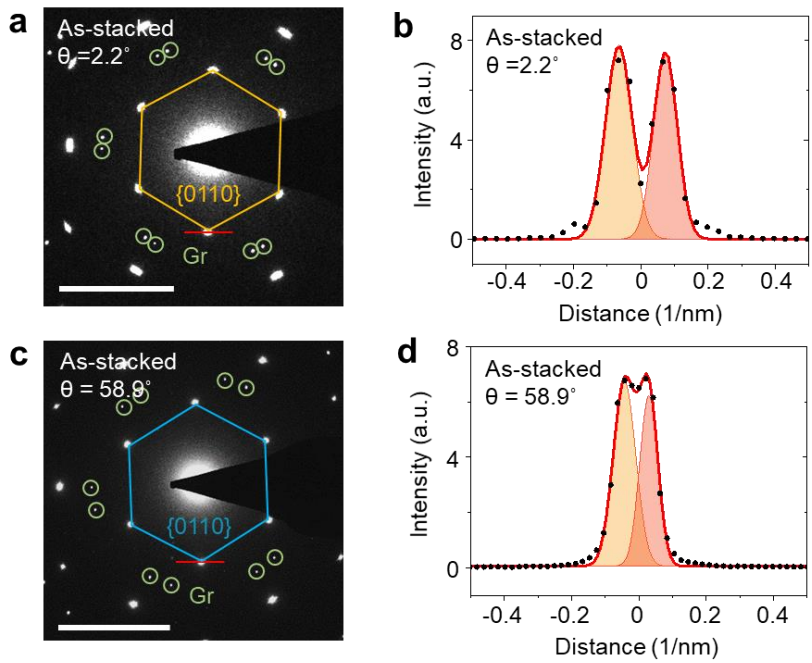

Figure 22. (a) SAED images of graphene-encapsulated R-stack $WSe_2/MoSe_2$ before annealing. Scale bar: 5 nm^{-1}. (b) Line profiles of SAED collected from red solid lines in **a**. Black dot represents the raw data. (c) SAED images of graphene-encapsulated R-stack $WSe_2/MoSe_2$ before annealing. Scale bar: 5 nm^{-1}. (d) Line profiles of SAED collected from red solid lines in **a**. Black dot represents the raw data. Two samples are the same samples in **Fig. 20**

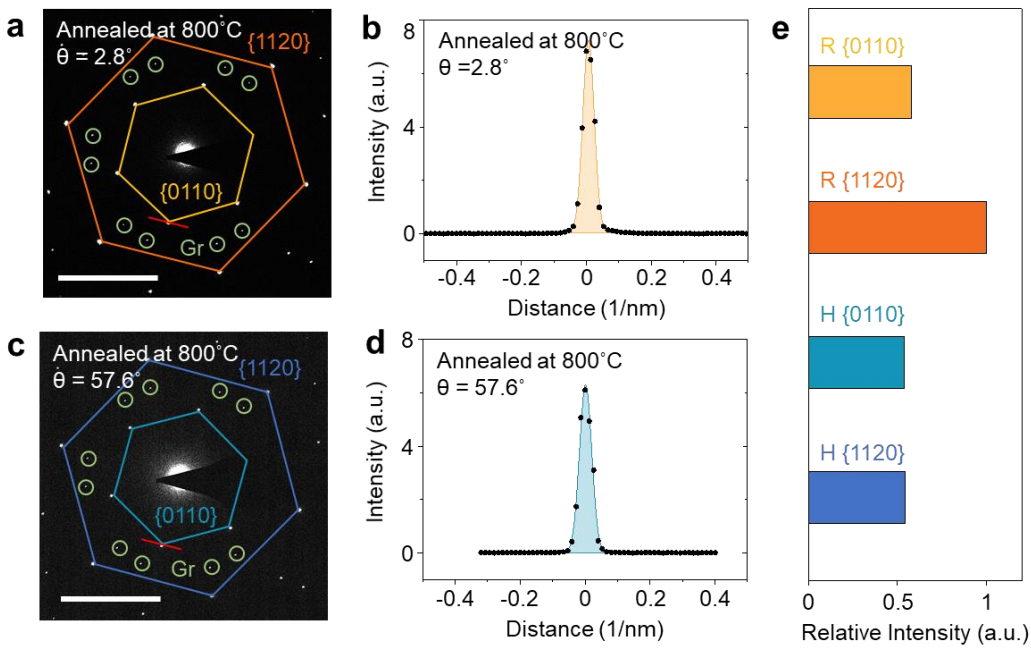

Figure 23. (a) SAED images of graphene-encapsulated R-FC $WSe_2/MoSe_2$ after annealing. Scale bar: 5 nm^{-1}. (b) Line profiles of SAED collected from red solid lines in **a**. Black dot represents the raw data. (c) SAED images of graphene-encapsulated R-stack $WSe_2/MoSe_2$ before annealing. Scale bar: 5 nm^{-1}. (d) Line profiles of SAED collected from red solid lines in **a**. Black dot represents the raw data. (e) Average of the relative intensity of {0110} and {1120} lattice planes from R- and H-type FC. Two samples are the same samples in **Fig. 21**

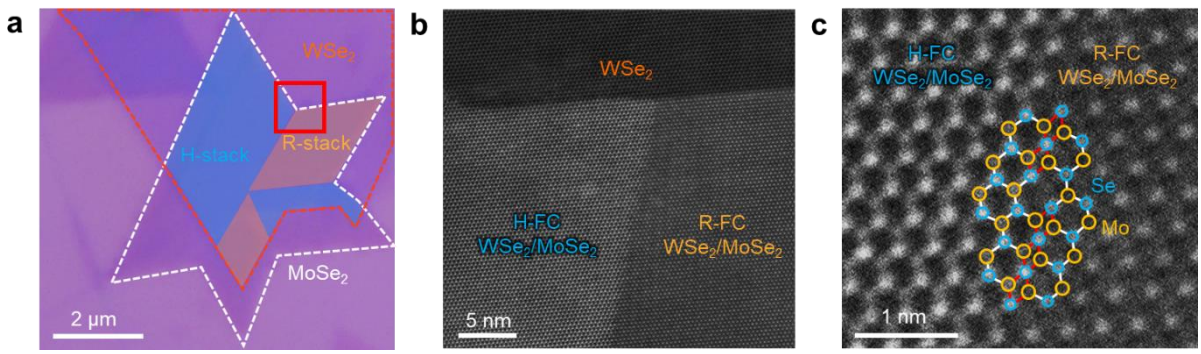

Figure 24. (a) Optical image of twisted $WSe_2/MoSe_2$ consisted of polycrystalline $MoSe_2$ and single crystal WSe_2. False-colored regions represent different stacking type of hetero-bilayers: R-stack (orange) and H-stack (blue). (b) HAADF-STEM image of partially overlapped regions single crystal WSe_2 and polycrystalline $MoSe_2$. Inset shows the e, Magnified HAADF-STEM images of the red box in Fig. 3D. Circles represent the Mo (orange) and Se (blue) atoms and red rhombuses represent mirror twin boundaries of $MoSe_2$.

Dependence of twist angle on the atomic reconstruction

Interlayer interactions in twisted TMD bilayers depend on the twist angle and can be characterized by interlayer shear modes (SM) and breathing modes (LBM) in low-frequency (LF) Raman spectroscopy. These interlayer Raman modes exhibit variations with the twist angle and polytypes of TMD bilayers, such as the 3R and 2H phases. Given the limited research on TMD hetero-bilayers using LF Raman spectroscopy, I investigated the LF Raman spectra of homo-structures of WSe_2 to verify the dependence of the twist angle on the atomic configuration of FC structures. These materials have been extensively studied for their interlayer Raman modes, providing valuable insights into the atomic structure FC-TMDs. As shown in LF Raman spectra of epitaxially grown 3R- and 2H-WSe_2 bilayer (Fig. 25), they show two significant LF Raman peaks of SM and LBM modes, while any peaks Ire detected from 1L-WSe_2. The intensity ratio between SM and LBM peaks is clearly different by their structural phase. In the hBN-encapsulated WSe_2 bilayers, LBM peaks exhibited a blueshift and peak splitting, and several unknown LBM peaks Ire emerged between SM and LBM peaks. This difference is attributed to the interlayer coupling between capping hBN layers and WSe_2. To investigate the dependence of twist angle on the atomic configuration of FC structures, I fabricated several WSe_2/WSe_2 homo-bilayers with various twist angle. In as-stacked homo-bilayers, the SM and LBM Raman peaks varied depending on the twist angle, resulting from

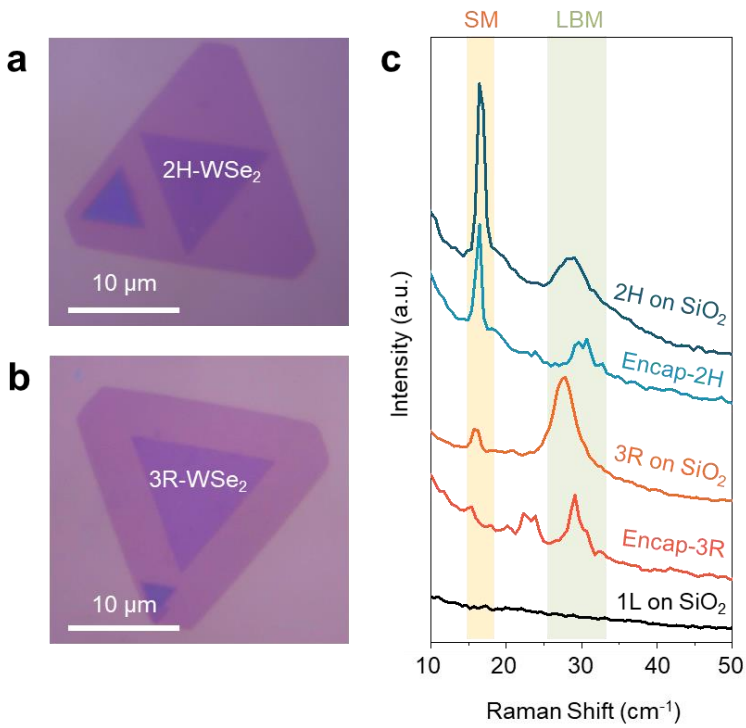

Figure 25. (a,b) Optical images of CVD-grown 2H (a) and 3R (b) phase WSe_2 bilayers. (c) Low-frequency Raman spectra of 1L- and 2L-WSe_2 on SiO_2/Si substrate and encapsulated with hBN.

different interlayer coupling behavior at different twist angles (Fig. 26). However, after annealing WSe_2/WSe2 homo-bilayers at 950˚C, the SM and LBM peaks of R-stack WSe_2 homo-bilayers (15.5˚ and 28.8˚) Ire observed to be similar to those of CVD-grown 3R WSe_2, while the H-stack homo-bilayers (47.1˚ and 58.8˚) exhibited similarities to the CVD-grown 2H WSe_2. It implies that the R-stack TMD bilayers ($0^\circ < \theta < 30^\circ$) converted into the 3R structure, while H-stack ($30^\circ < \theta < 60^\circ$) into 2H, regardless of the initial twist angle. Thus, these LF Raman results support the selective formation of R- and H-FC TMD layers.

The R- and H-FC structures exhibit different PL features of interlayer excitons. Because the 3R structure is non-centrosymmetric structure unlike centrosymmetric 2H structure, spontaneous electric polarization in out-of-plane direction exists in 3R-TMDs (Figs. 27a-b). The interlayer exciton in WSe_2/$MoSe_2$ hetero-bilayer also has electric dipole moment in out-of-plane direction due to localization of holes and electrons in WSe_2 and $MoSe_2$, respectively. Therefore, the intrinsic polarization can induce PL shifts of interlayer excitons in R-FC bilayers (Fig. 27c).

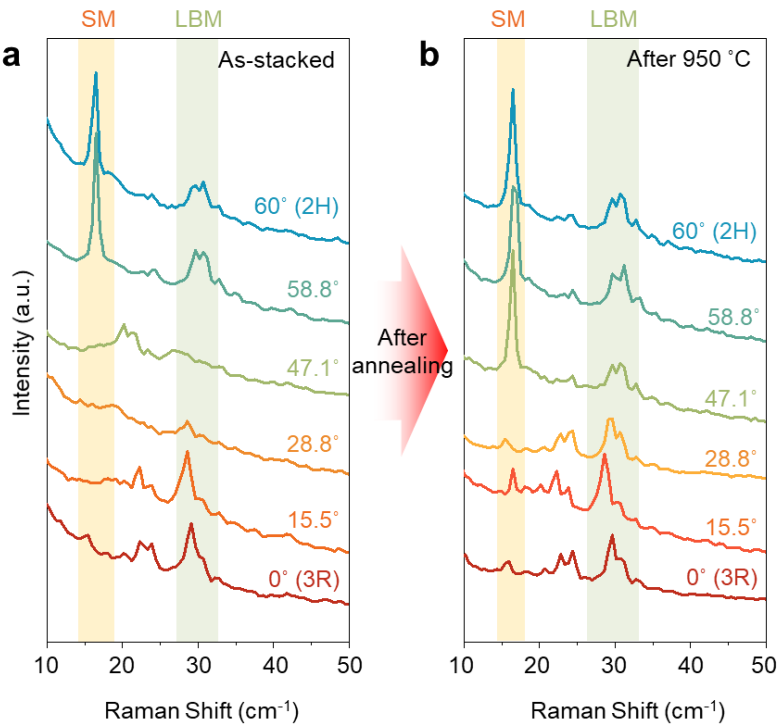

Figure 26. (a,b) Low-frequency Raman spectra of artificially stacked WSe_2 homo-bilayers encapsulated with hBN as-stacked (a) and after annealing (b) at 950˚C for 1 h. The spectra of 0˚ and 60˚ Ire obtained from flakes in **Fig. 25**.

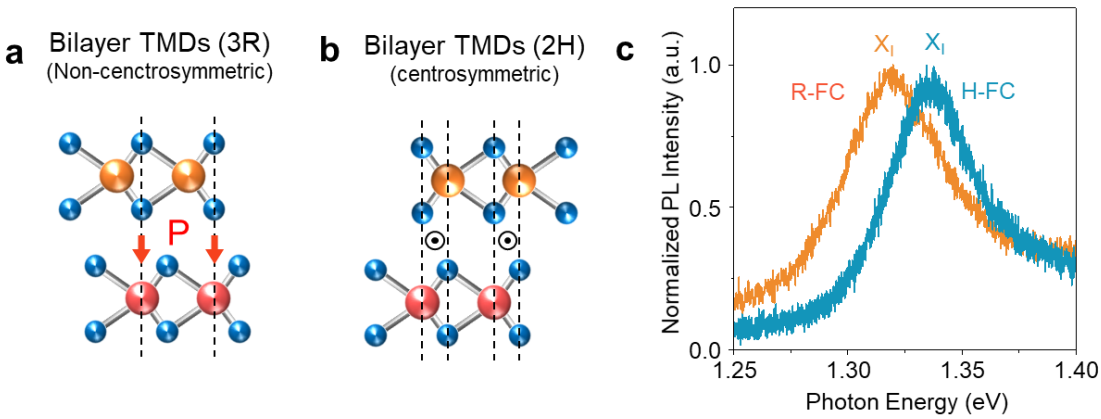

Figure 27. (a,b) Schematic images of atomic structures of 3R (a) and 2H (b) phase TMD bilayers. Circles represent metal (Red and orange) and chalcogen (blue) atoms. Intrinsic polarization exists in non-centrosymmetric 3R phase through a direction of chalcogen to metal atoms. Center of inversion symmetry in 2H phase is represented by black circles. (c) Normalized PL spectra of R-FC and H-FC $WSe_2/MoSe_2$ after annealing at 800˚C. Orange and blue lines represent R-FC and H-FC respectively.

4.4. Conclusion

In this chapter, I demonstrated the controlled formation of zero-twisted and lattice-matched FC structures through encapsulation annealing of TMD hetero-bilayers by using CVD-grown TMDs. Fig. 28 summarizes an overview of the self-reconstruction and thermally induced reconstruction by the twist angle of twisted TMD layers. The total van der Waals (vdW) energy of the TMD bilayers as a function of the twist angle, calculated in Ref.27, presents the twist-angle-dependent stability of the moiré heterostructure and reconstructed phases (Fig. 28a). When the twist angle of R-stack and H-stack bilayers is below the critical angle (θ_c), which is close to 0˚ and 60˚, self- reconstruction occurs in TMD bilayers to minimize the total vdW energy, leading to the formation of periodic domains separated by incommensurate (IC) boundaries, as illustrated in Figs 28b and 28c. The atomic structure of the reconstructed domains depends on the stacking sequence: R-stack to the 3R configuration, while H-stack to the 2H configuration. Meanwhile, when twist angle is larger than θ_c, the twisted TMD bilayers maintain moiré superlattices due to the lack of sufficient thermal energy at room temperature to overcome the energy barrier for spontaneous atomic reconstruction (Fig. 28d). Nevertheless, encapsulation annealing of the twisted TMD bilayers over critical temperature results in atomic reconstruction into the FC structures of Figs. 28e and 28f, regardless of the twist angle and stacking type. I verified that the R-stack and H-stack twisted TMD bilayers reconstructed into 3R and 2H structure, respectively. Thus, the atomic configuration of FC structures can be controlled by the initial stacking types of the TMD bilayers. The selective formation of specific FC structures opens up possibilities for tailored material properties and device functionalities.

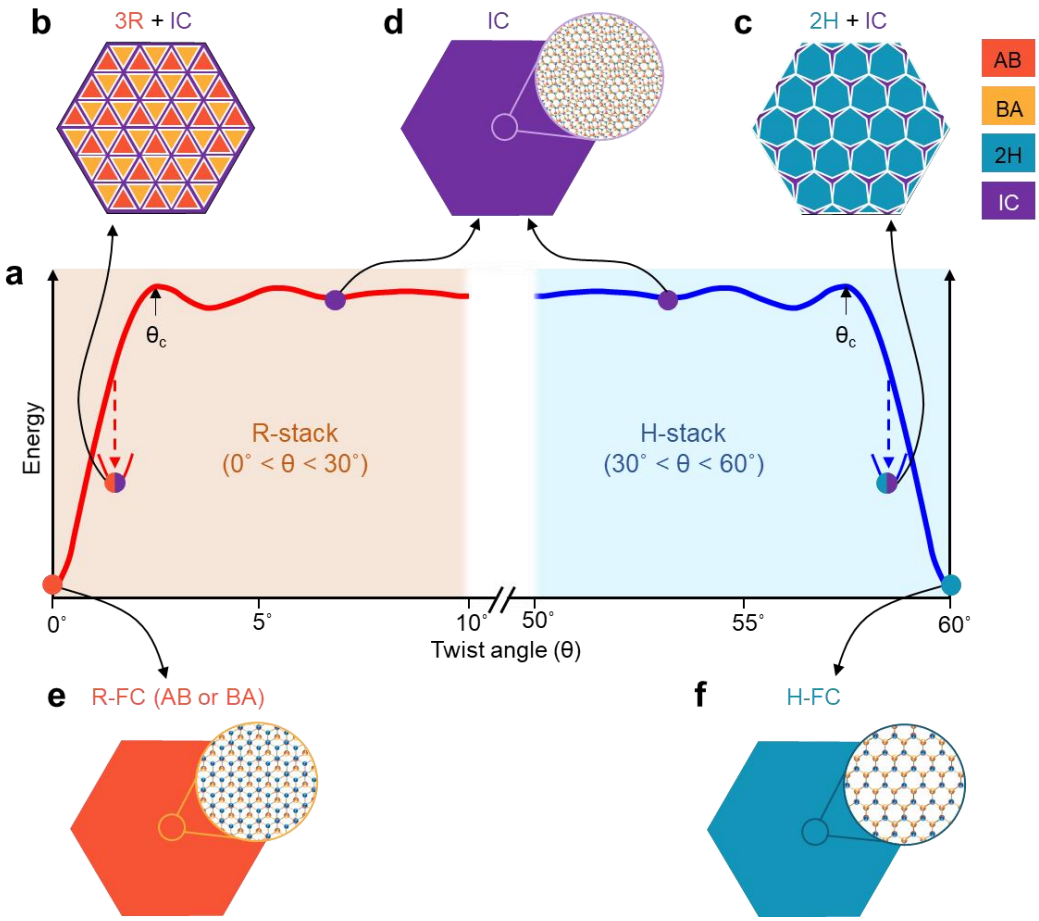

Figure 28. (a) Schematics of total vdW energy of twisted TMD bilayers as a function of twist angle. (b-f) Schematic illustrations of atomic structure of twisted TMDs by their stacking type and twist angle before (b-d) and after annealing (e,f). Orange, yellow, blue, and purple domains represent the AB (3R), BA (3R), 2H, and incommensurate (IC) respectively. Red, orange, blue circles represent W, Mo, Se atoms respectively.

Chapter 5. Atomic Reconstruction in Twisted Two-dimensional Layers with Large Lattice Mismatch

5.1. Introduction

In previous chapters, I demonstrated the thermally induced atomic reconstruction in randomly stacked TMD layers. However, it is confined on the small-mismatched hetero-bilayers and lattice-matched homo-layers, where a slight expansion or contraction of lattice structures is required to formation of fully commensurate (FC) structures. In this chapter, I investigate the atomic reconstruction in hetero-bilayers with large lattice mismatch, such as $MoS_2/MoSe_2$ and WS_2/WSe_2. The lattice mismatch of them is approximately 4% (*79, 80*), which presents a challenge for achieving self-reconstruction and atomic alignment (*14, 81, 82*). Previous research on epitaxially grown WS_2/WSe_2 hetero-bilayers has shown an impossibility of self-reconstruction due to a large lattice mismatch, even at near-zero twist angles (*14*). To investigate the atomic reconstruction in large-mismatched hetero-bilayers, I performed encapsulation annealing at 1100˚C, a higher temperature than that required for inducing atomic reconstruction in homo-bilayers of TMDs. After annealing, I observed the alignment of crystalline orientations between MoS_2 and $MoSe_2$, indicating the occurrence of atomic reconstruction which exhibits distinct features compared to small-mismatched TMD bilayers.

5.2. Methods

Sample preparation

Flakes of hBN, Gr Ire mechanically exfoliated from bulk crystals onto SiO_2/Si substrates. Monolayer TMD flakes Ire grown by chemical vapor deposition (CVD) methods. The thickness of monolayer TMDs Ire identified by optical contrast, photoluminescence (PL) measurements, and atomic force microscopy. The vdW heterostructures Ire fabricated by traditional pick-up transfer method with PC/PDMS films.

Transmission electron microscopy

HAADF-STEM images and SAED patterns Ire acquired Cs-corrected-monochromated TEM/STEM (Themis Z) at an operating voltage of 80 kV with a probe current of 30 pA, a 25 mrad convergence angle, and a collection angle range of 84-200 mrad.

Raman spectroscopy

Low-frequency Raman spectra Ire acquired using Raman spectroscopy (Horiba LabRAM HR Evolution) with a 532 nm laser and a spot size of ~ 1 μm. Angle-resolved Raman spectra Ire acquired using Raman spectroscopy (JASCO) with a 532 nm laser and a spot size of ~1 μm. The Raman and PL spectra Ire obtained at the same position before and after annealing.

5.3. Results and Discussion

I investigated atomic structures of stacked $MoS_2/MoSe_2$ hetero-bilayers where the lattice mismatch between MoS_2 and $MoSe_2$ is ~4%. In near-zero stacked $MoS_2/MoSe_2$ ($\theta = 59.3^\circ$), the self-reconstruction was not observed due to large lattice mismatch despite of near-zero twist angle of 59.3˚ (Fig. 29). It is consistent with previous reported results in epitaxially grown WS_2/WSe_2 hetero-bilayers (*14*). As shown in SAED profiles of $MoS_2/MoSe_2$ projected as a direction of $(0\bar{1}10)$ lattice plane (Fig. 30), positions of SAED peaks of hetero-bilayers Ire obtained same as monolayer regions of MoS_2 and $MoSe_2$. It indicates that the atomic reconstruction did not occur in large-mismatched hetero-bilayers despite of near-zero twist angle of 59.3˚. However, after $MoS_2/MoSe_2$ ($\theta = 34.8^\circ$) hetero-bilayers are encapsulation-annealed at 1100˚C, which is a higher temperature than the required temperature to induce the atomic reconstruction in homo-bilayers of MoS_2/MoS_2 and $MoSe_2/MoSe_2$, I verified that the atomic reconstruction occurred in $MoS_2/MoSe_2$. As shown in SAED images of $MoS_2/MoSe_2$ after annealing (Figs. 31a-c), I observed the alignment of crystalline orientations of MoS_2 and $MoSe_2$. However, $MoS_2/MoSe_2$ hetero-bilayers show different features compared with small-mismatched TMD bilayers, where two distinct SAED peaks Ire observed in the $MoS_2/MoSe_2$ regions (Figs. 31d-e). The d-spacing at peak 1 of the hetero-bilayer corresponds precisely to the average value between the d-spacing of MoS_2 and $MoSe_2$. It implies that this peak 1 is formed by the deformation of both MoS_2 and $MoSe_2$ during reconstruction process. As shown in high magnification HAADF-STEM images of reconstructed $MoS_2/MoSe_2$ (Figs. 32a-c), I observed a mixed structure consisting

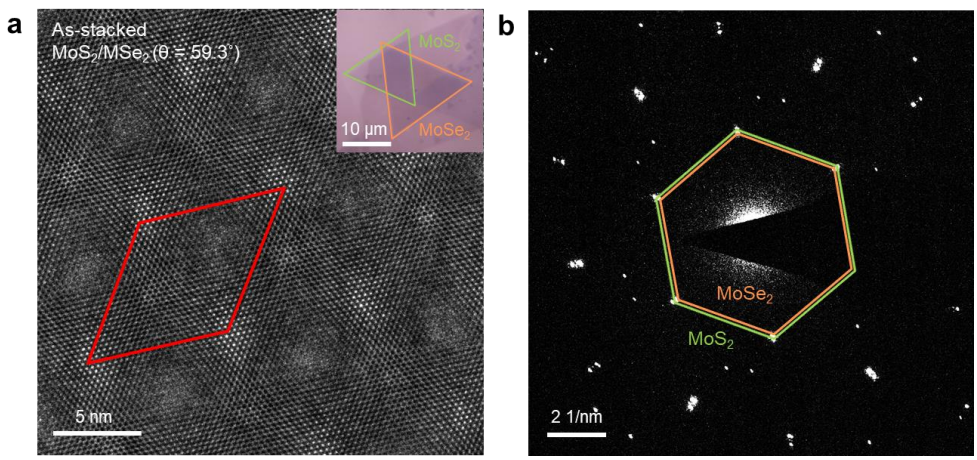

Figure 29. (a) HAADF-STEM images of the as-stacked $MoS_2/MoSe_2$ hetero-bilayer (θ = 59.3˚). Red rhombus represents a unit cell of moiré superlattices. Inset shows optical image of graphene-encapsulated $MoS_2/MoSe_2$ hetero-bilayer. (b) SAED image of as-stacked $MoS_2/MoSe_2$ hetero-bilayer.

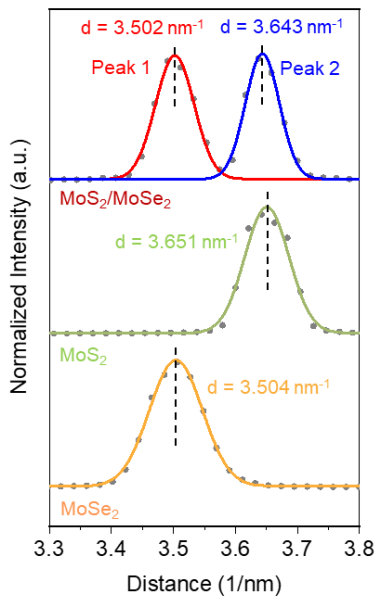

Figure 30. SAED profiles of $MoS_2/MoSe_2$ hetero-bilayer and monolayer regions of MoS_2 and $MoSe_2$, projected as a direction of $(0\bar{1}10)$ lattice plane.

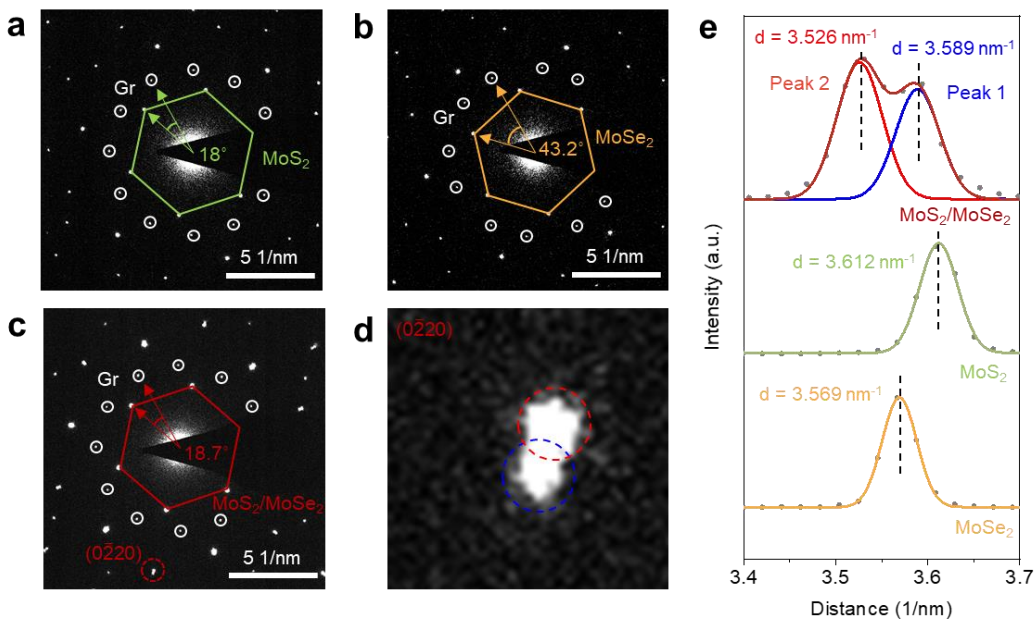

Figure 31. (a-b) SAED images of monolayer regions of MoS_2 (a) and $MoSe_2$ (b) after annealing at 1100˚C. (c) SAED images of the $MoS_2/MoSe_2$ hetero-bilayer after annealing at 1100˚C. Crystalline orientation of TMDs are defined with respect to relative angle with Gr. (d) Magnified SAED images for the $(0\bar{2}20)$ lattice plane from red circles in **c**. (e) SAED profiles of $MoS_2/MoSe_2$ hetero-bilayer and monolayer regions of MoS_2 and $MoSe_2$, projected as a direction of $(0\bar{1}10)$ lattice plane. Peaks 1 and 2 correspond to the dashed circles in **d**.

of commensurate (2H) and aligned incommensurate regions (AIC), explaining the observation of two SAED peaks. Note that this AIC structure is different from the saddle point (SP) regions that are normally observed in self-reconstructed hetero-bilayers. The SP regions in the self-reconstructed hetero-bilayers have the misorientation between two layers as shown in Fig. 20 and previous studies (*28, 83*).

As shown in low-frequency (LF) Raman spectra of $MoS_2/MoSe_2$ (Fig. 33a), the emergence of LF Raman peaks after annealing at 1100˚C supports the occurrence of the atomic reconstruction. However, Raman spectra of $MoS_2/MoSe_2$ at the high-frequency regimes becomes highly broaden after annealing at 1100˚C, indicating the degradation of TMDs (Fig. 33b). The representative Raman peaks of MoS_2 Ire red-shifted after annealing. The A_{1g} and E^1_{2g} peaks exhibit a redshift of 5.26 and 10.1 cm^{-1}, respectively, indicating that in-plane tensile strain of 2% is applied on MoS_2 (Fig. 34a). Moreover, the peak intensity of A_{1g} and E^1_{2g} peaks show any dependence on the polarization direction of incident light (Fig. 34b). It indicates the in-plane biaxial strain is applied on the MoS_2, whereas a uniaxial strain induces a twofold or fourfold polarization angle dependence on the Raman peak intensity. In contrast to $MoS_2/MoSe_2$, I cannot observe the atomic reconstruction in WS_2/WSe_2 even annealing at 1100˚C, which is the temperature limit of our furnace, as shown in STEM images and Raman spectra of Fig. 35. This might be due to exceptionally strong atomic bonding of WS_2.

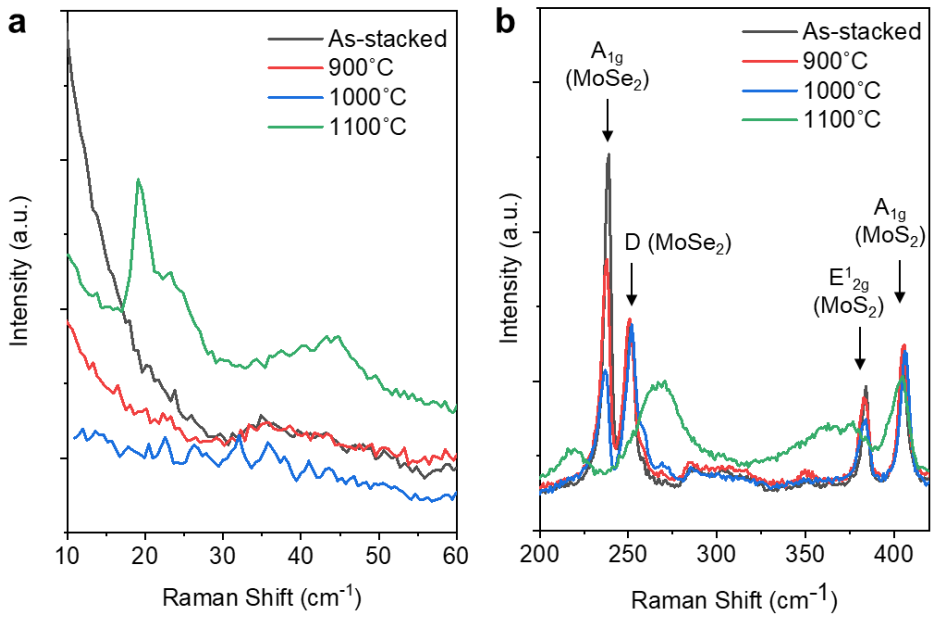

Figure 33. (a,b) Raman spectra of the $MoS_2/MoSe_2$ hetero-bilayer at low-frequency (a) and high-frequency (b) regimes by increasing annealing temperature.

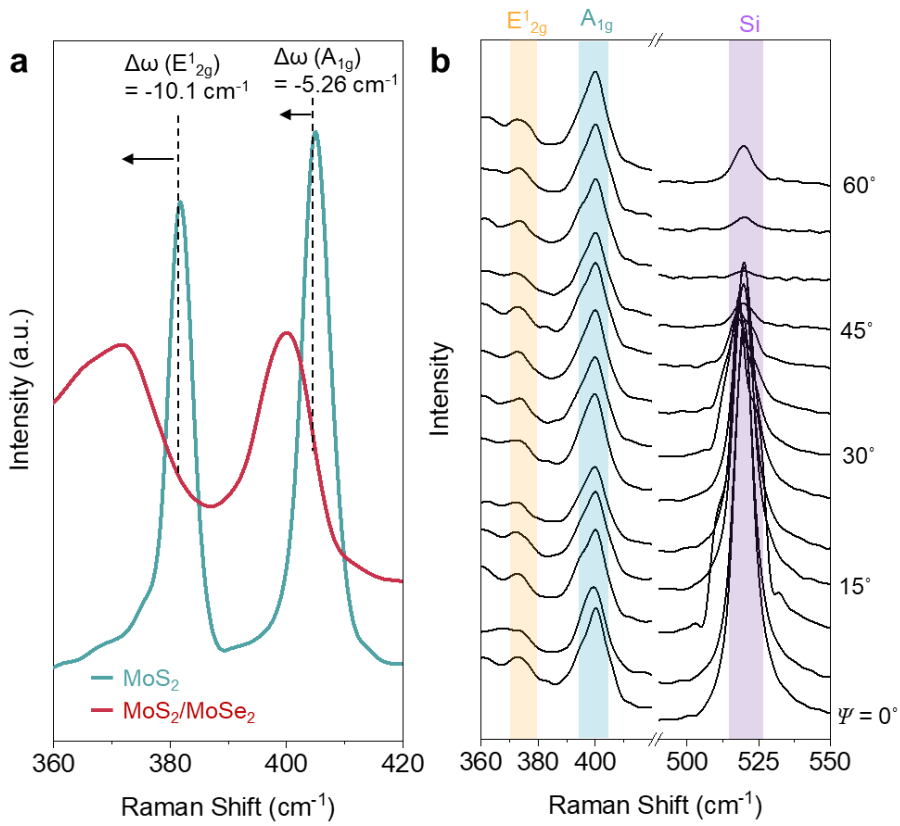

Figure 34. (a) Raman spectra of the $MoS_2/MoSe_2$ hetero-bilayer and monolayer regions of MoS_2 after annealing at 1100˚C. Both of two representative Raman peaks of MoS_2 show redshift ($\Delta\omega$) after annealing. (b) Angle-resolved Raman spectra of the $MoS_2/MoSe_2$ hetero-bilayer after annealing.

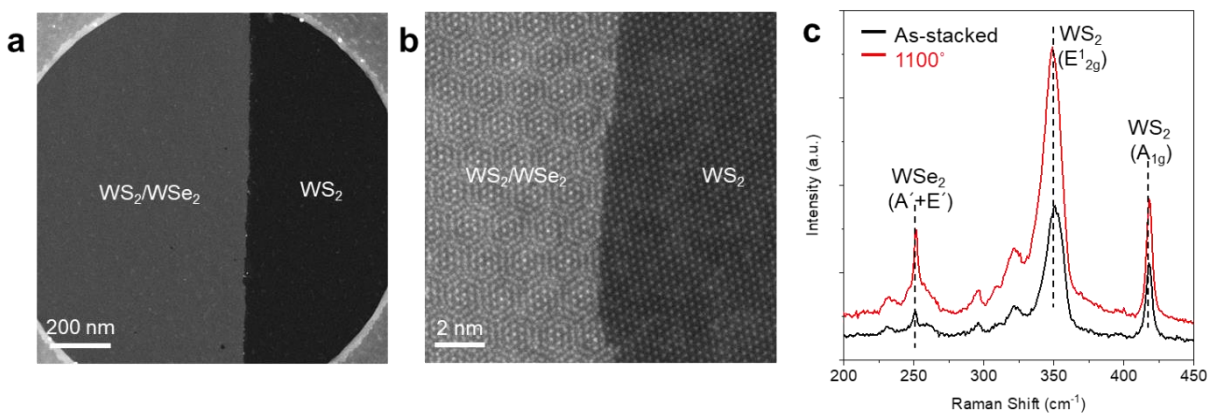

Figure 35. (a,b) HAADF-STEM images of the WS_2/WSe_2 hetero-bilayer after annealing at 1100˚C in low-magnification (a) and high-magnification (b). (c) Raman spectra of the WS_2/WSe_2 hetero-bilayer before and after annealing at 1100˚C

5.4. Conclusion

In conclusion, I investigated the atomic reconstruction in large-mismatched hetero-bilayers, specifically $MoS_2/MoSe_2$ and WS_2/WSe_2 systems. I demonstrate that despite a significant lattice mismatch of approximately 4%, atomic alignment, and reconstruction were achieved in $MoS_2/MoSe_2$ through encapsulation annealing at 1100˚C. However, WS_2/WSe_2 hetero-bilayers did not exhibit atomic reconstruction even after annealing at the temperature of 1100˚C, possibly due to the stiffness of the atomic bonding in WS_2. Our findings elucidate the possibility of achieving atomic reconstruction in large-mismatched hetero-bilayers and contribute to the understanding of interlayer interactions in TMDs. These insights have implications for the design and development of advanced electronic and optoelectronic devices based on TMD heterostructures.

Chapter 6. Revealing Mechanism of Atomic Reconstruction via *in-situ* Scanning Tunneling Transmission Electron Microscopy

6.1. Introduction

I developed novel approaches for the formation of fully commensurate (FC) structures of TMD bilayers *via* encapsulation annealing. However, a mechanism of atomic rearrangement during reconstruction is elusive. In this chapter, to elucidate the mechanism of the thermally induced atomic reconstruction in twisted TMD bilayers, I investigated in-situ STEM of $WSe_2/MoSe_2$ and WSe_2/WSe_2 twisted-bilayers by applying short duration of heating pulses (< 2 sec) of different temperature (400~1000˚C). I have discovered a sequential rotational ordering of crystal lattices, resulting in the formation of nanoscale-aligned domains in twisted TMD bilayers. These aligned domains exhibit growth through a local atomic rearrangement within the moiré supercells, accompanied by the hopping of 5|7 defect pairs at the boundaries of the moiré patterns. Our observations of this distinct atomic reconstruction phenomenon in 2D moiré heterostructures provide valuable insights into the intricate atomic-scale interactions.

6.2. Experimental procedures

Sample preparation

The hBN, Gr Ire mechanically exfoliated from bulk crystals onto SiO_2/Si substrates. Monolayer TMD flakes Ire grown by chemical vapor deposition (CVD) methods. The thickness of monolayer TMDs Ire identified by optical contrast, photoluminescence (PL) measurements, and atomic force microscopy. The vdW heterostructures Ire fabricated by traditional pick-up transfer method with PC/PDMS films. To prevent the degradation of heterostructures during annealing, bi- or tri-layer graphene Ire is used. However, since it is difficult to detach the graphene from the SiO_2/Si substrate due to stronger adhesion force between Gr/SiO_x rather than hBN/SiO_x, hBN used as top layer to easily detach the graphene. Thus, hBN/Gr/TMDs bilayer/Gr heterostructures Ire fabricated at first. Next, a XeF_2 gas, which can selectively etch only the hBN remaining in the graphene, was treated on the heterostructures to remove the top hBN. TEM samples Ire prepared by using a poly (methyl methacrylate) (PMMA)-based It transfer method. Samples on PMMA film Ire transferred on MEMS-based heating chips (Protochips, E-FHDN-VO-10), and the PMMA film was removed by placing samples in acetone for 24 hours.

Transmission electron microscopy

The samples Ire imaged in a Thermo Fisher Scientific Themis Z aberration-corrected (S)TEM. The aberration-corrected ADF-STEM images and DFTEM images Ire obtained using the STEM and TEM capabilities of the instrument, respectively. The microscope was operated at 80 kV to minimize knock-on damage of the 2D materials. A convergence angle of 25.2 mrad was used to obtain the images.

In-situ heating

The samples Ire deposited to MEMS-based chips for the *in-situ* heating experiments. A heating holder (Fusion Select, Protochips) was used to apply heat pulses of 0.5s from 100°C to 1000°C. DFTEM and/or ADF-STEM images Ire acquired after each 0.5s heat pulse was applied and the samples Ire quenched to room temperature. The temperatures for DFTEM images series are 100°C to 400°C at 100°C temperature steps and 400°C to 1000°C at 50°C temperature steps. The temperatures for ADF-STEM imaging are 400°C to 900°C at 100°C temperature steps.

6.3. Results and discussion

I prepared Gr-encapsulated TMD bilayers on microelectromechanical-system (MEMS) based E-chips for in-situ heating experiments (Fig. 36a). To obtain atomic-resolution images of intermediate structures during atomic reconstruction, I applied short-duration heating pulses to the TMD bilayers, followed by imaging with STEM at room temperature after rapid cooling. The temperature profile is illustrated in Fig. 36b. By increasing the temperature of heating pulses, the atomic reconstruction in $MoSe_2/WSe_2$ (θ = 41.8˚) was observed upon applying the heating pulse of 900˚C (Fig. 37). This result is consistent with the emergence of interlayer exciton PL peaks as the annealing temperature increase (Fig. 4b). Due to the short duration of heating pulses, the critical temperature for inducing atomic reconstruction is obtained as higher than 800˚C. For the WSe2/WSe2 homo-bilayer (θ = 45.0˚), heating pulses of 1000˚C for 0.5 s resulted in the observation of partially reconstructed 2H domains surrounded by incommensurate (IC) moiré superlattices (Fig. 37). This clear evidence suggests that the atomic reconstruction through encapsulation annealing is attributed to the local rearrangement of atoms rather than the rotation of entire TMD flakes. Notably, I observed a seamless boundary between reconstructed domains and the IC domain, where 5|7 defect pairs Ire present (Fig. 38a). These 5|7 defect pairs Ire also observed in the monolayer regions of MoSe2 in the MoSe2/WSe2 hetero-bilayer (θ = 41.8˚) (Fig. 38b). Furthermore, by applying additional heating pulses ranging from 400˚C to 900˚C, I confirmed the propagation of grain boundaries between locally reconstructed domains and IC regions (Fig. 39a). The use of short heating pulses enabled accurate measurement of a migration of the boundary and the 5|7 defects. Discrete migration

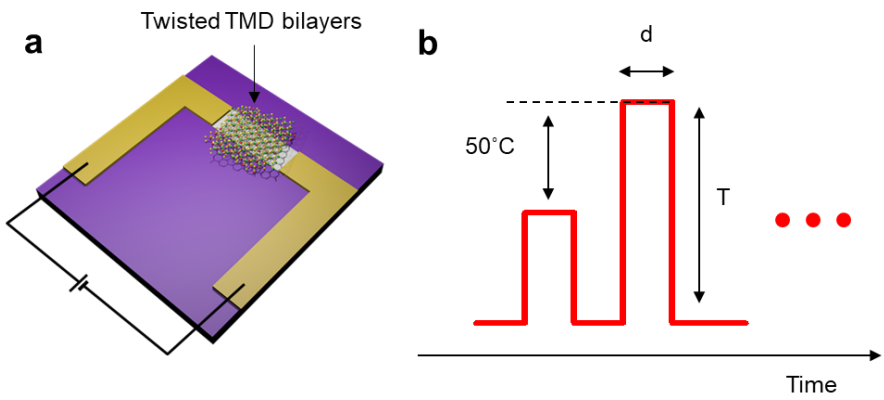

Figure 36. **a**, Schematic illustration of the twisted TMD bilayers on the *in-situ* heating chip. (b) Temperature profiles for *in-situ* heating pulses by modulating heating parameters (duration (*d*) and temperature (*T*)).

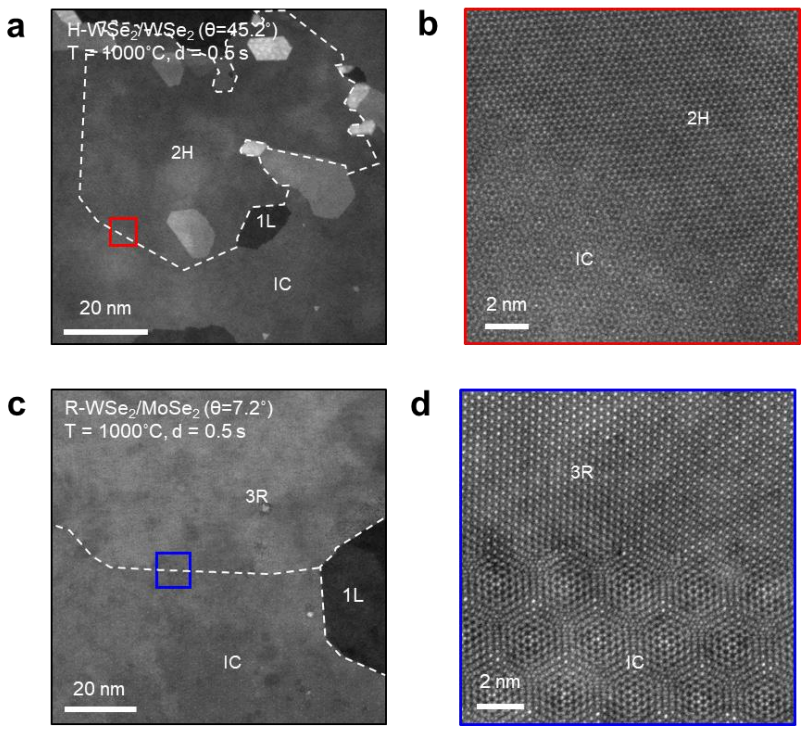

Figure 37. (a,b) HAADF-STEM images of the H-stack WSe_2/WSe_2 homo-bilayer (θ = 45.2˚) after applying a short heating pulse (T = 1000˚C and d = 0.5 s). (a,b) HAADF-STEM images of the R-stack $WSe_2/MoSe_2$ hetero-bilayer (θ = 7.2˚) after applying a short heating pulse (T = 1000˚C and d = 0.5 sec).

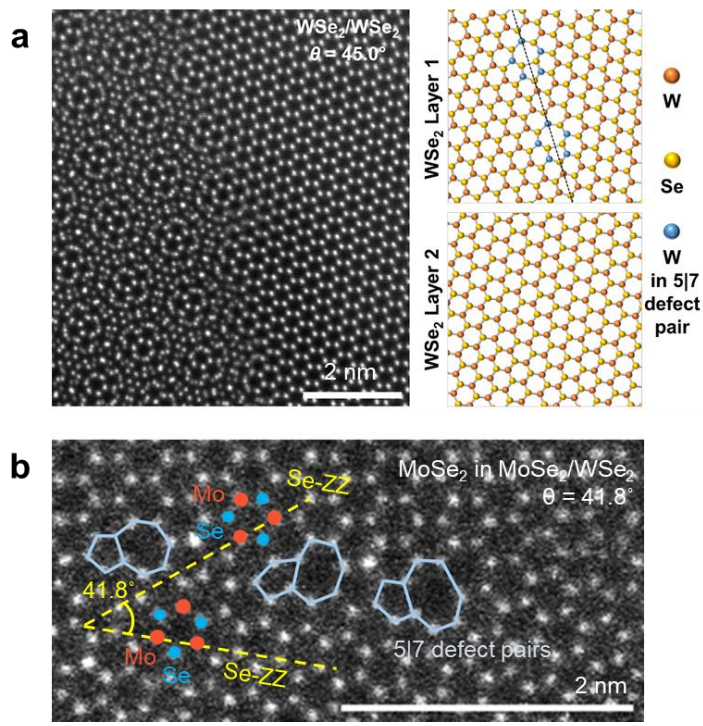

Figure 38. (a) (Left) Fourier-filtered HAADF-STEM image of the locally reconstructed WSe_2/WSe_2 homo-bilayer after applying short heating pulses. (Right) Atomic structures of grain boundary 5|7 defect pairs in WSe_2 monolayer 1 and pristine WSe_2 monolayer. (b) HAADF-STEM image of 5|7 defect pairs in 1L-$MoSe_2$ regions after applying short heating pulses.

of boundary was observed following heating pulses of 500, 600, and 700°C (Figs. 39b). The hopping-like migration of 5|7 defects to equivalent sites of adjacent moiré supercells resulted in the reconstruction of the moiré supercell into aligned structures. This hopping-like migration of the domain boundary represents a distinct mechanism compared to the continuous gliding of defect pairs observed in monolayer TMDs (*84-87*).

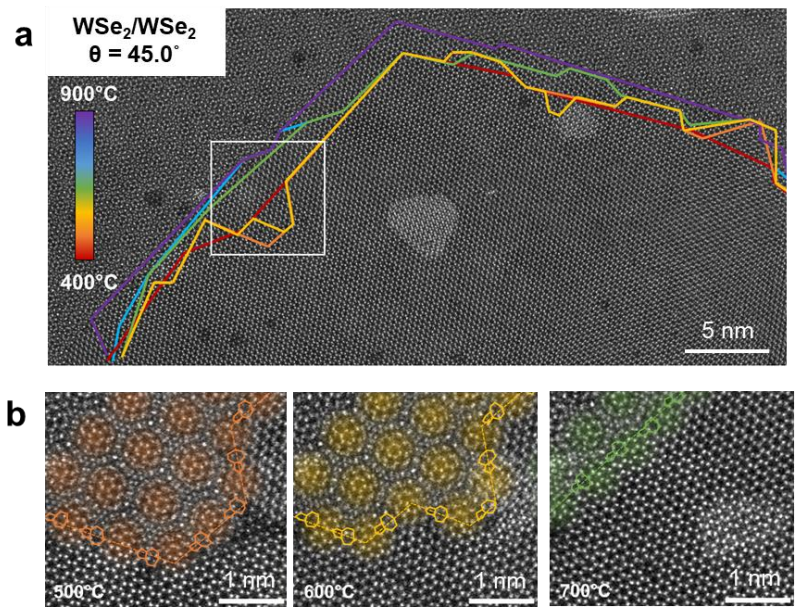

Figure 39. (a) HAADF-STEM image of the WSe_2/WSe_2 homo-bilayer (θ = 45.0˚) moiré-antiparallel interface at 900°C in twisted WSe_2/WSe_2 homo-bilayer. Colored lines mark the position of the moiré interface from 400˚C to 900˚C. (b–d) Magnified HAADF-STEM images of the interface from the region marked with the white box in **a**, after heat pulses of 500°C, 600°C, and 700°C. Dashed colored lines mark the positions of the interface.

6.4. Conclusion

In conclusion, our in-situ heating experiments on TMD bilayers have provided valuable insights into the dynamics of atomic reconstruction and its implications for the structural properties of these materials. By applying short-duration heating pulses and subsequent imaging techniques, I have observed the local rearrangement of atoms and the migration of grain boundaries, leading to the formation of aligned structures and the presence of defect pairs. These findings elucidated the mechanism of atomic reconstruction in driving the structural transformations. Importantly, our results demonstrate that the atomic reconstruction process is not caused by the rotation of entire TMD flakes but atomic rearrangements at the local level. This understanding opens up new possibilities for tailoring the properties of TMD-based materials through controlled manipulation of their atomic structure.

Chapter 7. Improvement of Interfacial Ferroelectricity in 3R phase of Transition Metal Dichalcogenides

7.1. Introduction

Recently, the ferroelectric property in rhombohedral phase (3R) TMDs bilayers was reported both theoretically and experimentally due to the inversion symmetry breaking, while the net electrical polarization in the 2H phase is zero due to the presence of the inversion symmetry (*88-93*). The intrinsic electrical polarization direction of 3R-TMDs is determined by a stacking sequence of metal and chalcogen atoms in upper and lower TMDs layers (Fig. 40). Here, I investigated a permanent electric polarization switching in the fully commensurate (FC) 3R-WSe_2 bilayers by applying an external electric field, inducing transition from AB stacking to BA stacking. I demonstrated that FC-WSe_2 exhibits good ferroelectric properties due to structural homogeneity of FC structures compared with near-zero twisted WSe_2 bilayers which exhibit inhomogeneous periodic structures. A large coercive field of 0.266 V/nm and polarization of 34.6 pC/m was obtained from R-FC WSe_2. Moreover, a long retention time (>10^4 s) and high ferroelectric transition temperature (437 K) Ire obtained, while near-zero (NZ) stacked 3R-WSe_2 shows short retention time (~ 10^2 s) and low transition temperature (353 K) due to the presence of incommensurate domains. The structural homogeneity of FC-WSe_2 contributed to the stability of ferroelectric polarization states. These findings provide valuable insights into the ferroelectric properties of FC-WSe_2 bilayers and their potential for future applications in ferroelectric devices.

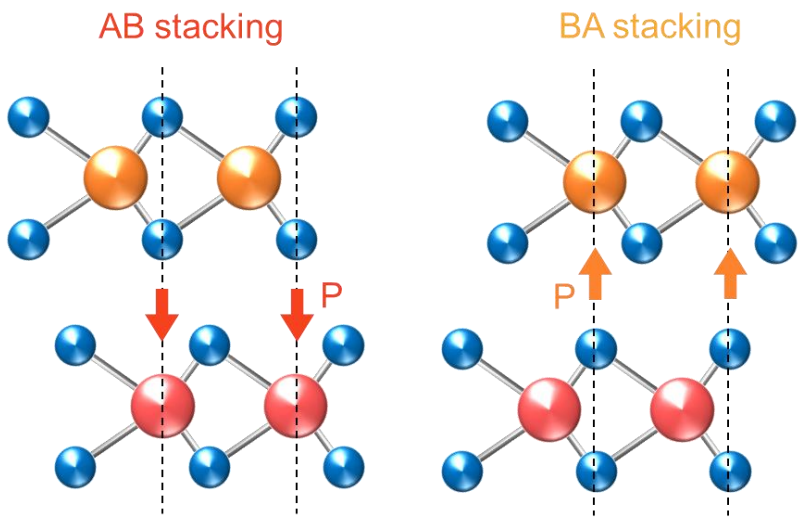

Figure 40. Schematic of the intrinsic polarization of AB and BA stacking of 3R-TMDs. Direction of electric polarization in 3R-TMDs is represented by arrows.

7.2. Experimental procedures

Sample preparation

Flakes of hBN, Gr Ire mechanically exfoliated from bulk crystals onto SiO_2/Si substrates. Monolayer TMD flakes Ire grown by chemical vapor deposition (CVD) methods. The thickness of monolayer TMDs Ire identified by optical contrast, photoluminescence (PL) measurements, and atomic force microscopy. The vdW heterostructures Ire fabricated by traditional pick-up transfer method with PC/PDMS films. To form R-FC WSe_2 structures, vdW heterostructures Ire annealed at 900˚C for 1 h. Electrodes of devices Ire patterned by using an e-beam lithography and Cr/Pd/Au (1/30/30 nm) metal electrodes Ire deposited by using an e-beam evaporator.

Raman and PL spectroscopy

Low-frequency Raman spectra Ire acquired using Raman spectroscopy (Horiba LabRAM HR Evolution) with a 532 nm laser and a spot size of ~ 1 μm. Angle-resolved Raman spectra Ire acquired using Raman spectroscopy (JASCO) with a 532 nm laser and a spot size of ~ 1 μm. The Raman and PL spectra Ire obtained at the same position before and after annealing.

Electrical measurements

The electrical measurements of the devices Ire performed using a parameter analyzer (Keithley 4200) under vacuum conditions (< 10 mtorr).

7.3. Results and discussion

As shown in Fig. 41a, I fabricated field-effect transistor (FET) with graphene (Gr) channel on hexagonal boron nitride (hBN) gate dielectric, and R-stack WSe_2 bilayer, which have parallel alignment of crystalline orientation of two constituent layers, Ire embedded in hBN layers. To easily estimate the stacking type of WSe_2 bilayers, I used triangular WSe_2 flakes synthesized by a chemical vapor deposition (CVD) method. The mesoscopic atomic structure of R-stack WSe_2 is determined by twist angle of two WSe_2 layers. When two flakes of 1L-WSe_2 are stacked with near-zero (NZ) twist angle, triangular domains of AB and BA are formed alternately (Fig. 41b). In the AB stacking, every chalcogen atom on the top layer is located over the metal atom on the bottom layer, and vice versa in the BA stacking. In the case of large twist angle, twisted WSe_2 bilayers construct moiré superlattices as well known. However, when hBN-encapsulated R-stack WSe_2 are annealed at 900˚C for 1h, I demonstrated that R-stack WSe_2 bilayers reconstructed into R-FC WSe_2 bilayers which have an ideal 3R atomic structure without any incommensurate (IC) regions regardless of their twist angle (Fig. 26). To investigate the ferroelectricity of NZ-R and R-FC WSe_2, I fabricated two devices as shown in Fig. 42. As I expected the transfer curve of Gr on hBN did not show hysteresis loop (Fig. 42b), however, the curve of Gr on NZ-R WSe_2 show hysteresis loop (Fig. 42b). It is attributed to that an area of AB or BA domains can be modulated by applying external out-of-plane electric field*94*), since the M and X atoms are aligned along the direction of the external electric field to reduce the electrical potential energy. However, about 10^2 s of short retention time was measured from NZ-R WSe_2 (Fig. 42d), because IC regions in NZ-R WSe_2 serve as a seed of restoration of the flipped domains after

removing external electric field. Unlike NZ-R WSe_2, the transfer curve from R-FC WSe_2 showed significant hysteresis loop, while Gr on hBN did not show any ferroelectric behaviors (Figs. 42f-g). The coercive field of R-FC WSe_2 was roughly measured as 0.266 V/nm, and electrical polarization (P_{FC}) was calculated as 34.6 pC/m from the simple parallel capacitance model (Fig. 43) (*93*),

$$n = \frac{C}{e} \cdot V_{Dirac} \tag{4}$$

$$n_f - n_b = 2\Delta n_p = \frac{C}{e} (V_{Dirac,f} - V_{Dirac,b}) \tag{5}$$

$$P_{FC} = e\Delta n_p t_{di} \tag{6}$$

where n is the carrier concentration, C is the dielectric capacitance, e is the elementary charge, V_{Dirac} is the charge neutral point of Gr channel, and $t_{di}$is the thickness of the dielectric. Meanwhile, the lower value of polarization from NZ-WSe_2 (P_{NZ}) was obtained as 10.3 pC/m. This difference is attributed to the limited ferroelectric transition in NZ-WSe_2 due to the presence of topological defects. Moreover, as shown in Fig. 42h, I obtained long retention time over 10^4 s from R-FC WSe_2 because of their homogeneous structure without any IC domains which can initiate the restoration of AB/BA transition. Fig. 43 displays the temperature dependence of the ferroelectricity of the R-FC WSe_2. Although temperature was increased up to 437 K, the transfer curve of Gr on R-FC WSe2 showed clear hysteresis loop (Figs. 41a-b). However, the hysteresis loop disappeared when the transfer curve was measured above 456 K (Figs. 41c). The Curie temperature of R-FC WSe2 was roughly measured as 437 K. This high ferroelectric temperature of R-FC WSe_2 is attributed to the thermodynamically stable structures of polarized states. This value corresponds to the theoretically calculated ferroelectric transition temperature of 3R-TMDs (*94*). Moreover, it is a quite reasonable value by comparing

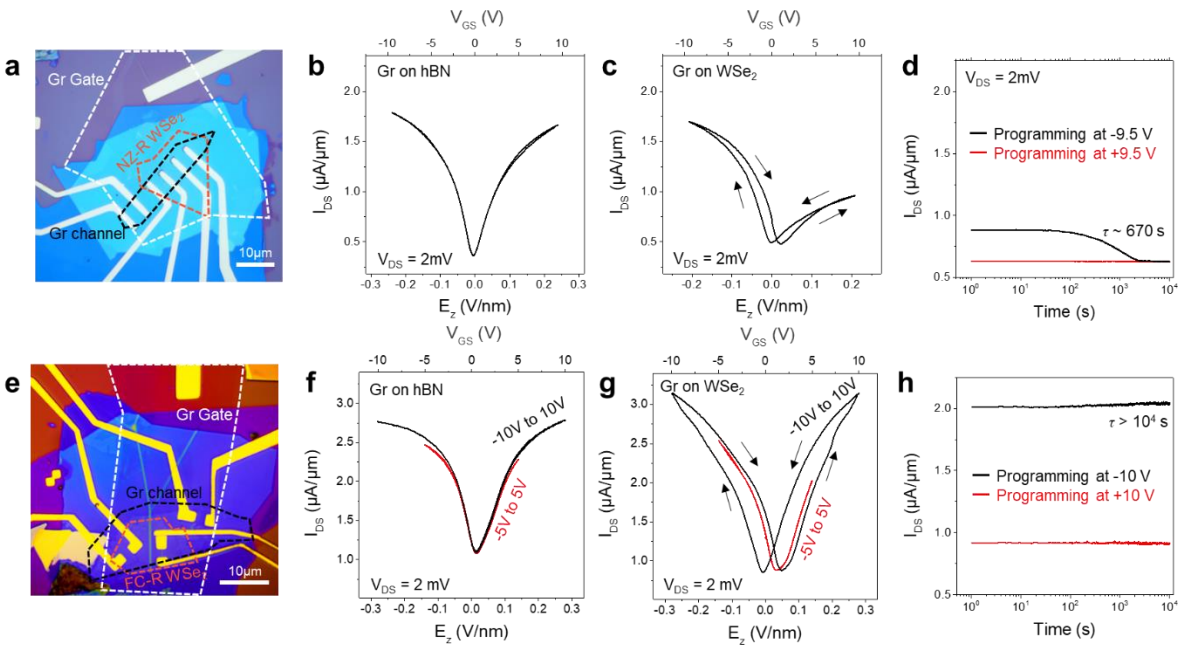

Figure 42. (a) Optical image of Gr-FET on NZ-R WSe_2. (b,c) Transfer characteristics of Gr-FET on the hBN (b) and NZ-R WSe_2 (c). (d) Retention measurement for Gr-FET on NZ-R WSe_2 after programming at ±9.5 V. (e) Optical image of Gr-FET on FC-R WSe_2. (f,g) Transfer characteristics of Gr-FET on the hBN (f) and FC-R WSe_2 (g). (h) Retention measurement for Gr-FET on FC-R WSe_2 after programming at ±10 V.

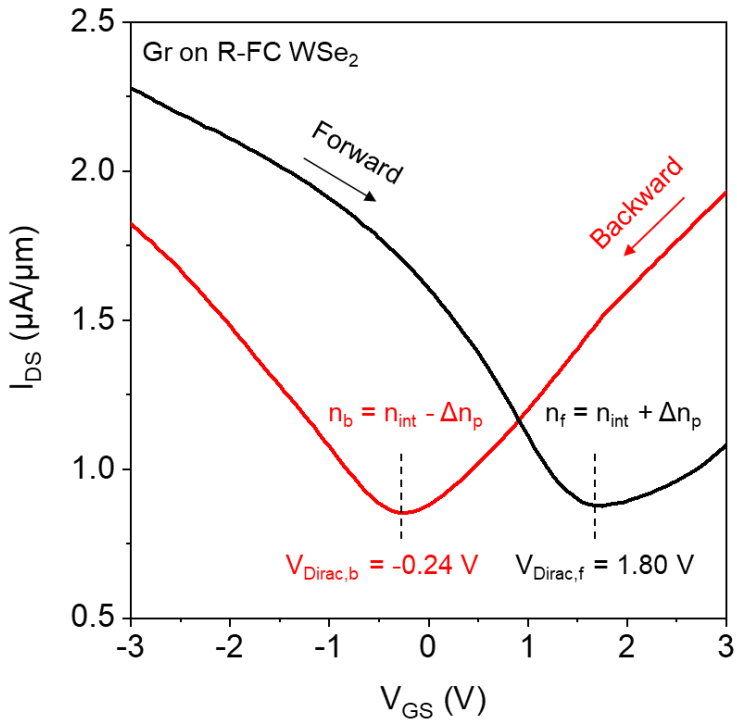

Figure 43. Dirac voltage (V_{Dirac}) of the Gr-FET on R-FC WSe_2. Carrier concentration at Dirac point (n_f and n_b) is defined by a sum of intrinsic charge concentration (n_{int}) of graphene and polarization-induced charge concentration (Δn_p), and characterized by simple parallel capacitance model.

well-known ferroelectric materials, such as a poly (vinylidene fluoride) (PVDF) which polarization of 6.7 μC/cm^2 and Curie temperature of 468 K (*95*, *96*). I observed that difference of the charge neutral point (ΔV_{CNP}) of Gr channel on R-FC WSe_2 abruptly decreased over 164˚C which indicates the ferroelectric transition. The FC-WSe_2 exhibits first-order ferroelectric transition as a function of temperature due to abrupt sliding transition between AB and BA structures. Meanwhile, NZ-WSe_2 shows second-order ferroelectric transition because of gradual change of net polarization in NZ-WSe_2 by the external electric field (*93*). Therefore, the structural homogeneity of FC structures contributes to the stability of ferroelectric polarization states, resulting in the long retention, high polarization value, and high ferroelectric transition temperature.

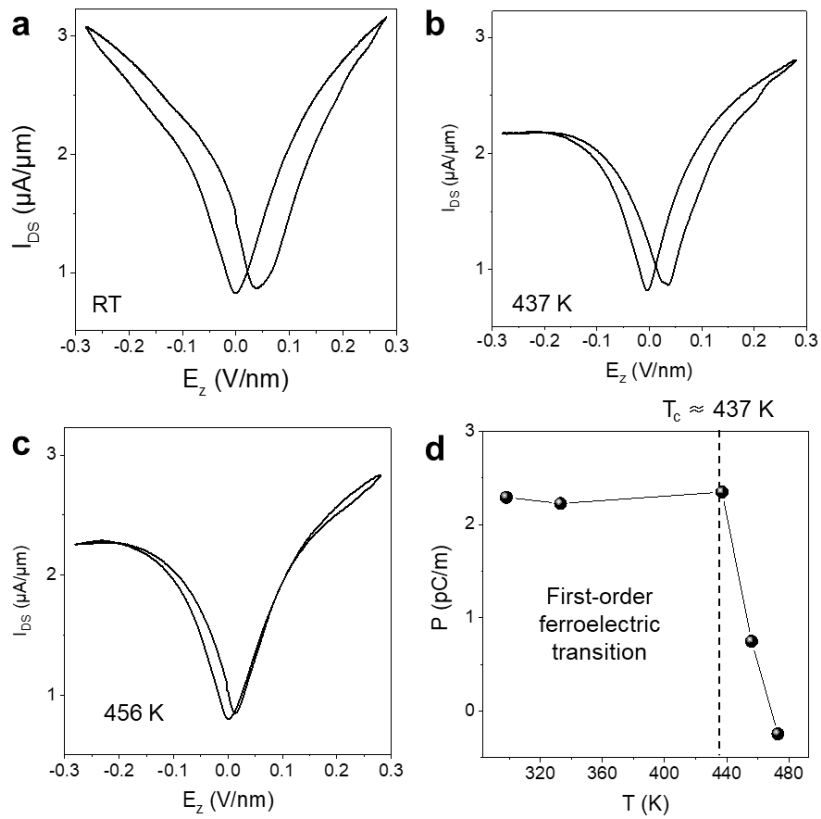

Figure 44. (a-c) Transfer characteristics of Gr-FET on R-FC WSe_2 with increasing temperature to room temperature (a), 437 (b), and 456 K (c). (d) Calculated electric polarization of R-FC WSe_2 by eq. (6) as a function of temperature.

7.4. Conclusion

In conclusion, our study focused on investigating the ferroelectric properties of FC and NZ-stacked WSe_2 bilayers. The FC-WSe_2 exhibited excellent ferroelectric properties attributed to its structural homogeneity, while NZ-WSe_2 demonstrated limitations due to the presence of incommensurate domains. I observed polarization switching in the NZ-R WSe_2 bilayers by applying an external electric field, indicating their ferroelectric behavior. In contrast, the transfer curve of Gr on FC-WSe_2 showed a significant hysteresis loop, confirming its ferroelectric nature. Furthermore, FC-WSe_2 exhibited a higher ferroelectric transition temperature compared to NZ-WSe_2, indicating a first-order ferroelectric transition in the former and a second-order transition in the latter. The structural homogeneity of FC-WSe_2 contributed to the stability of ferroelectric polarization states, resulting in a longer retention time and higher polarization values. These findings provide valuable insights into the ferroelectric properties of FC-WSe_2 bilayers and their potential for future applications in ferroelectric devices. Further research and exploration in this field can lead to the development of novel materials and technologies for advanced electronic and optoelectronic applications.

Chapter 8. Conclusion

In this thesis, I reported a novel method for achieving FC structures by thermally inducing atomic reconstruction in randomly stacked TMD layers using encapsulation annealing. Our approach resulted in the formation of zero-twisted and lattice-matched FC structures, regardless of the initial twist angles and lattice mismatches. The atomic structure of FC structures can be controlled by the stacking 2D layers with either parallel (R-stack) or anti-parallel (H-stack) alignment of the constituent TMD layers. This approach resulted in the formation of zero-twisted and lattice-matched FC structures, regardless of the initial twist angles and lattice mismatches. I have demonstrated that the stacking type of the constituent TMD layers, whether in a parallel (R-stack) or anti-parallel (H-stack) configuration, can be utilized to control the atomic structure of FC structures. Moreover, I have investigated the challenges and observations in achieving self-reconstruction in large-mismatched hetero-bilayers, further expanding the scope of our methodology. Importantly, our method allows for the controllable formation of FC structures with any desired combination of TMDs without epitaxial growth. Furthermore, I elucidated the atomic-scale mechanisms of atomic reconstruction by *in-situ* STEM imaging, sequential rotational ordering and formation of nanoscale-aligned domains through local atomic rearrangement. Owing to structural homogeneity of FC structures, I verified the improvement of interfacial sliding ferroelectricity of R-FC TMD bilayers compared with near-zero stacked TMD bilayers, in which separated domains surrounded by topological defects exists. Overall, this work contributes to the understanding of formation of FC structures of TMD layers and their implications for novel physical phenomena and potential applications. With the

controllable formation of FC structures and the improved interfacial properties observed, our work paves the way for future advancements and developments in the field of TMD heterostructures.

Bibliography

1. A. K. G. K. S. Novoselov, S. V. Morozov, D. Jiang, Y. Zhang, S. V. Dubonos, I. V. Grigorieva, A. A. Firsov, Electric Field Effect in Atomically Thin Carbon Films. *Science* **306**, 666-669 (2004).
2. G. Giovannetti, P. A. Khomyakov, G. Brocks, P. J. Kelly, J. van den Brink, Substrate-induced band gap in graphene on hexagonal boron nitride:Ab initiodensity functional calculations. *Phys. Rev. B* **76**, (2007).
3. K. F. Mak, C. Lee, J. Hone, J. Shan, T. F. Heinz, Atomically thin MoS_2: a new direct-gap semiconductor. *Phys. Rev. Lett.* **105**, 136805 (2010).
4. A. K. Geim, I. V. Grigorieva, Van der Waals heterostructures. *Nature* **499**, 419-425 (2013).
5. C. H. Lee *et al.*, Atomically thin p-n junctions with van der Waals heterointerfaces. *Nat. Nanotechnol.* **9**, 676-681 (2014).
6. K. S. Novoselov, A. Mishchenko, A. Carvalho, A. H. Castro Neto, 2D materials and van der Waals heterostructures. *Science* **353**, aac9439 (2016).
7. H. Fang *et al.*, Strong interlayer coupling in van der Waals heterostructures built from single-layer chalcogenides. *Proc. Natl. Acad. Sci. USA* **111**, 6198-6202 (2014).
8. Y.-Y. Wang, F.-P. Li, W. Wei, B.-B. Huang, Y. Dai, Interlayer coupling effect in van der Waals heterostructures of transition metal dichalcogenides. *Frontiers of Physics* **16**, (2020).
9. W. Wan *et al.*, Interlayer coupling of a direct van der Waals epitaxial MoS_2/graphene heterostructure. *RSC Adv.* **6**, 323-330 (2016).
10. L. Liang *et al.*, Low-Frequency Shear and Layer-Breathing Modes in Raman Scattering of Two-Dimensional Materials. *ACS Nano* **11**, 11777-11802 (2017).
11. Y. Cao *et al.*, Unconventional superconductivity in magic-angle graphene superlattices. *Nature* **556**, 43-50 (2018).
12. Y. Cao *et al.*, Correlated insulator behaviour at half-filling in magic-angle graphene superlattices. *Nature* **556**, 80-84 (2018).
13. S. Carr *et al.*, Twistronics: Manipulating the electronic properties of two-dimensional layered structures through their twist angle. *Physi. Rev. B* **95**, (2017).
14. L. Yuan *et al.*, Twist-angle-dependent interlayer exciton diffusion in WS_2-WSe_2 heterobilayers. *Nat. Mater.* **19**, 617-623 (2020).
15. M. Liao *et al.*, Twist angle-dependent conductivities across MoS_2/graphene heterojunctions. *Nat. Commun.* **9**, 4068 (2018).
16. P. Rivera *et al.*, Interlayer valley excitons in heterobilayers of transition metal dichalcogenides. *Nat. Nanotechnol.* **13**, 1004-1015 (2018).
17. H. Yu, G.-B. Liu, W. Yao, Brightened spin-triplet interlayer excitons and optical selection rules in van der Waals heterobilayers. *2D Mater.* **5**, (2018).
18. Y. Tang *et al.*, Tuning layer-hybridized moire excitons by the quantum-confined Stark effect. *Nat. Nanotechnol.* **16**, 52-57 (2021).
19. Y. Bai *et al.*, Excitons in strain-induced one-dimensional moiré potentials at transition metal dichalcogenide heterojunctions. *Nat. Mater.* **19**, 1068-1073 (2020).
20. Y. Shimazaki *et al.*, Strongly correlated electrons and hybrid excitons in a

moire heterostructure. *Nature* **580**, 472-477 (2020).
21. L. Wang *et al.*, Correlated electronic phases in twisted bilayer transition metal dichalcogenides. *Nat. Mater.* **19**, 861-866 (2020).
22. K. Tran *et al.*, Evidence for moiré excitons in van der Waals heterostructures. *Nature* **567**, 71-75 (2019).
23. C. Jin *et al.*, Observation of moire excitons in WSe_2/WS_2 heterostructure superlattices. *Nature* **567**, 76-80 (2019).
24. E. C. Regan *et al.*, Emerging exciton physics in transition metal dichalcogenide heterobilayers. *Nat. Rev. Mater.* **7**, 778-795 (2022).
25. K. F. Mak, J. Shan, Semiconductor moiré materials. *Nat. Nanotechnol.* **17**, 686-695 (2022).
26. S. Zhu, P. Pochet, H. T. Johnson, Controlling Rotation of Two-Dimensional Material Flakes. *ACS Nano* **13**, 6925-6931 (2019).
27. H. Yoo *et al.*, Atomic and electronic reconstruction at the van der Waals interface in twisted bilayer graphene. *Nat. Mater.* **18**, 448-453 (2019).
28. A. Iston *et al.*, Atomic reconstruction in twisted bilayers of transition metal dichalcogenides. *Nat. Nanotechnol.* **15**, 592-597 (2020).
29. J. Holler *et al.*, Low-frequency Raman scattering in WSe_2–$MoSe_2$ heterobilayers: Evidence for atomic reconstruction. *Appl. Phys. Lett.* **117**, (2020).
30. M. R. Rosenberger *et al.*, Twist Angle-Dependent Atomic Reconstruction and Moiré Patterns in Transition Metal Dichalcogenide Heterostructures. *ACS Nano* **14**, 4550-4558 (2020).
31. J. Quan *et al.*, Phonon renormalization in reconstructed MoS_2 moiré superlattices. *Nat. Mater.* **20**, 1100-1105 (2021).
32. S. Zhu, H. T. Johnson, Moiré-templated strain patterning in transition-metal dichalcogenides and application in twisted bilayer MoS_2. *Nanoscale* **10**, 20689-20701 (2018).
33. S. Zhao *et al.*, Excitons in mesoscopically reconstructed moiré heterostructures. *Nat. Nanotechnol.* **18**, 572-579 (2023).
34. S. Zhang *et al.*, Domino-like stacking order switching in twisted monolayer-multilayer graphene. *Nat. Mater.* **21**, 621-626 (2022).
35. J. H. Kim *et al.*, Interface-Driven Partial Dislocation Formation in 2D Heterostructures. *Adv. Mater.* **31**, e1807486 (2019).
36. M. Kang *et al.*, Universal Mechanism of Band-Gap Engineering in Transition-Metal Dichalcogenides. *Nano. Lett.* **17**, 1610-1615 (2017).
37. Q. H. Wang, K. Kalantar-Zadeh, A. Kis, J. N. Coleman, M. S. Strano, Electronics and optoelectronics of two-dimensional transition metal dichalcogenides. *Nat. Nanotechnol.* **7**, 699-712 (2012).
38. T. Cao *et al.*, Valley-selective circular dichroism of monolayer molybdenum disulphide. *Nat. Commun.* **3**, 887 (2012).
39. C. Witteveen *et al.*, Polytypism and superconductivity in the NbS_2 system. *Dalton Trans.* **50**, 3216-3223 (2021).
40. Y. Li, K. A. Duerloo, K. Wauson, E. J. Reed, Structural semiconductor-to-semimetal phase transition in two-dimensional materials induced by electrostatic gating. *Nat. Commun.* **7**, 10671 (2016).
41. M. T. H. Terrones, Electronic and vibrational properties of defective transition metal dichalcogenide Haeckelites new 2D semi-metallic systems. *2D Mater.* **1**, 011003 (2014).

42. P. Li *et al.*, Evidence for topological type-II Weyl semimetal WTe_2. *Nat. Commun.* **8**, 2150 (2017).
43. Y. Deng *et al.*, $MoTe_2$: Semiconductor or Semimetal? *ACS Nano* **15**, 12465-12474 (2021).
44. J. Jiang *et al.*, Signature of type-II Weyl semimetal phase in $MoTe_2$. *Nat. Commun.* **8**, 13973 (2017).
45. S. Tongay *et al.*, Thermally driven crossover from indirect toward direct bandgap in 2D semiconductors: $MoSe_2$ versus MoS_2. *Nano Lett.* **12**, 5576-5580 (2012).
46. Y. Liu *et al.*, Van der Waals heterostructures and devices. *Nat. Rev. Mater.* **1**, (2016).
47. V. O. Özçelik, J. G. Azadani, C. Yang, S. J. Koester, T. Low, Band alignment of two-dimensional semiconductors for designing heterostructures with momentum space matching. *Phys. Rev. B* **94**, (2016).
48. Y. Jiang, S. Chen, W. Zheng, B. Zheng, A. Pan, Interlayer exciton formation, relaxation, and transport in TMD van der Waals heterostructures. *Light Sci. Appl.* **10**, 72 (2021).
49. J. P. Echeverry, B. Urbaszek, T. Amand, X. Marie, I. C. Gerber, Splitting between bright and dark excitons in transition metal dichalcogenide monolayers. *Phys. Rev. B* **93**, (2016).
50. F. Wu, F. Qu, A. H. MacDonald, Exciton band structure of monolayer MoS_2. *Phys. Rev. B* **91**, (2015).
51. D. Xiao, G. B. Liu, W. Feng, X. Xu, W. Yao, Coupled spin and valley physics in monolayers of MoS_2 and other group-VI dichalcogenides. *Phys. Rev. Lett.* **108**, 196802 (2012).
52. G. B. Liu, D. Xiao, Y. Yao, X. Xu, W. Yao, Electronic structures and theoretical modelling of two-dimensional group-VIB transition metal dichalcogenides. *Chem. Soc. Rev.* **44**, 2643-2663 (2015).
53. Z. Peng, X. Chen, Y. Fan, D. J. Srolovitz, D. Lei, Strain engineering of 2D semiconductors and graphene: from strain fields to band-structure tuning and photonic applications. *Light Sci. Appl.* **9**, 190 (2020).
54. L. Liu, T. Zhai, Wafer-scale vertical van der Waals heterostructures. *InfoMat* **3**, 3-21 (2020).
55. Y. Zhu *et al.*, Multiple roles of a heterointerface in two-dimensional van der Waals heterostructures: insights into energy-related applications. *J. Mater. Chem. A* **7**, 23577-23603 (2019).
56. Y. Liu, Y. Huang, X. Duan, Van der Waals integration before and beyond two-dimensional materials. *Nature* **567**, 323-333 (2019).
57. X. Cui *et al.*, Multi-terminal transport measurements of MoS_2 using a van der Waals heterostructure device platform. *Nat. Nanotechnol.* **10**, 534-540 (2015).
58. Y. Liu *et al.*, Toward barrier free contact to molybdenum disulfide using graphene electrodes. *Nano Lett.* **15**, 3030-3034 (2015).
59. T. Ye, J. Li, D. Li, Charge-Accumulation Effect in Transition Metal Dichalcogenide Heterobilayers. *Small* **15**, e1902424 (2019).
60. P. Rivera *et al.*, Observation of long-lived interlayer excitons in monolayer $MoSe_2$-WSe_2 heterostructures. *Nat. Commun.* **6**, 6242 (2015).
61. B. Kaviraj, D. Sahoo, Physics of excitons and their transport in two dimensional transition metal dichalcogenide semiconductors. *RSC Adv.* **9**,

25439-25461 (2019).
62. J. R. Schaibley *et al.*, Valleytronics in 2D materials. *Nat. Rev. Mater.* **1**, (2016).
63. L. Du *et al.*, Moiré photonics and optoelectronics. *Science* **379**, eadg0014 (2023).
64. C. R. Woods *et al.*, Charge-polarized interfacial superlattices in marginally twisted hexagonal boron nitride. *Nat. Commun.* **12**, 347 (2021).
65. M. O'Brien *et al.*, Mapping of Low-Frequency Raman Modes in CVD-Grown Transition Metal Dichalcogenides: Layer Number, Stacking Orientation and Resonant Effects. *Sci. Rep.* **6**, 19476 (2016).
66. J. U. Lee *et al.*, Strain-shear coupling in bilayer MoS_2. *Nat. Commun.* **8**, 1370 (2017).
67. K. Q. Lin *et al.*, Large-Scale Mapping of Moiré Superlattices by Hyperspectral Raman Imaging. *Adv. Mater.* **33**, e2008333 (2021).
68. F. Pizzocchero *et al.*, The hot pick-up technique for batch assembly of van der Waals heterostructures. *Nat. Commun.* **7**, 11894 (2016).
69. H. Ryu *et al.*, Anomalous Dimensionality-Driven Phase Transition of $MoTe_2$ in Van der Waals Heterostructure. *Adv. Funct. Mater.* **31**, (2021).
70. H. Rokni, W. Lu, Direct measurements of interfacial adhesion in 2D materials and van der Waals heterostructures in ambient air. *Nat. Commun.* **11**, 5607 (2020).
71. J. Son *et al.*, Atomically precise graphene etch stops for three dimensional integrated systems from two dimensional material heterostructures. *Nat. Commun.* **9**, 3988 (2018).
72. P. K. Nayak *et al.*, Probing Evolution of Twist-Angle-Dependent Interlayer Excitons in $MoSe_2/WSe_2$ van der Waals Heterostructures. *ACS Nano* **11**, 4041-4050 (2017).
73. L. Zhang *et al.*, Highly valley-polarized singlet and triplet interlayer excitons in van der Waals heterostructure. *Phys. Rev. B* **100**, (2019).
74. T. Wang *et al.*, Giant Valley-Zeeman Splitting from Spin-Singlet and Spin-Triplet Interlayer Excitons in $WSe_2/MoSe_2$ Heterostructure. *Nano Lett.* **20**, 694-700 (2020).
75. F. Cadiz *et al.*, Excitonic Linewidth Approaching the Homogeneous Limit in MoS_2-Based van der Waals Heterostructures. *Phys. Rev. X* **7**, 021026 (2017).
76. J. J. O. a. R. L. Longbothum, Empirical Fits to the Voigt Line Width: A Brief Review. *J. Quant. Spectrosc. Radiat. Transfer* **17**, 233-236 (1977).
77. A. Bala *et al.*, Large-Area MoS_2 Nanosheets with Triangular Nanopore Arrays as Active and Robust Electrocatalysts for Hydrogen Evolution. *J. Phys. Chem. C* **126**, 9696-9703 (2022).
78. S. Chen *et al.*, Origin of ultrafast growth of monolayer WSe_2 via chemical vapor deposition. *npj Comput. Mater.* **5**, 28 (2019).
79. A. L. W. G. Vandenberghe, Dielectric properties of mono- and bilayers determined from first principles. *2017 International Conference on Simulation of Semiconductor Processes and Devices (SISPAD)* (2017).
80. N. F. Q. Y. Yang Zhang, and Liang Fu, Moiré quantum chemistry charge transfer in transition metal dichalcogenide superlattices. Preprint at *arXiV:1910.14061v4* (2020).
81. C.-P. C. Chendong Zhang, Xibiao Ren, Ming-Yang Li, Lain-Jong Li,

Chuanhong Jin, Mei-Yin Chou, Chih-Kang Shih, Interlayer couplings, Moiré patterns, and 2D electronic superlattices in MoS_2/WSe_2 hetero-bilayers. *Sci. Adv.* **3**, e1601459 (2017).
82. T. Chen *et al.*, Lateral and Vertical $MoSe_2$-MoS_2 Heterostructures via Epitaxial Growth: Triggered by High-Temperature Annealing and Precursor Concentration. *J. Phys. Chem. Lett.* **10**, 5027-5035 (2019).
83. M. Van Winkle *et al.*, Rotational and dilational reconstruction in transition metal dichalcogenide moire bilayers. *Nat. Commun.* **14**, 2989 (2023).
84. A. Azizi *et al.*, Dislocation motion and grain boundary migration in two-dimensional tungsten disulphide. *Nat. Commun.* **5**, 4867 (2014).
85. X. Zou, M. Liu, Z. Shi, B. I. Yakobson, Environment-Controlled Dislocation Migration and Superplasticity in Monolayer MoS_2. *Nano Lett.* **15**, 3495-3500 (2015).
86. X. Zhao *et al.*, Healing of Planar Defects in 2D Materials via Grain Boundary Sliding. *Adv. Mater.* **31**, e1900237 (2019).
87. J. Chen *et al.*, In situ high temperature atomic level dynamics of large inversion domain formations in monolayer MoS_2. *Nanoscale* **11**, 1901-1913 (2019).
88. D. Yang *et al.*, Spontaneous-polarization-induced photovoltaic effect in rhombohedrally stacked MoS_2. *Nat. Photonics* **16**, 469-474 (2022).
89. L. W. Lukas Rogée, Yi Zhang, Songhua Cai, Peng Wang, Manish Chhowalla, Wei Ji, Shu Ping Lau, Ferroelectricity in untwisted heterobilayers oftransition metal dichalcogenides. *Science* **376**, 973-978 (2022).
90. S. Deb *et al.*, Cumulative polarization in conductive interfacial ferroelectrics. *Nature* **612**, 465-469 (2022).
91. X. Wang *et al.*, Interfacial ferroelectricity in rhombohedral-stacked bilayer transition metal dichalcogenides. *Nat. Nanotechnol.* **17**, 367-371 (2022).
92. P. Meng *et al.*, Sliding induced multiple polarization states in two-dimensional ferroelectrics. *Nat. Commun.* **13**, 7696 (2022).
93. Y. Liu, S. Liu, B. Li, W. J. Yoo, J. Hone, Identifying the Transition Order in an Artificial Ferroelectric van der Waals Heterostructure. *Nano Lett.* **22**, 1265-1269 (2022).
94. J. M. Marmolejo-Tejada, J. E. Roll, S. P. Poudel, S. Barraza-Lopez, M. A. Mosquera, Slippery Paraelectric Transition-Metal Dichalcogenide Bilayers. *Nano Lett.* **22**, 7984-7991 (2022).
95. H. Zhu, S. Yamamoto, J. Matsui, T. Miyashita, M. Mitsuishi, Ferroelectricity of poly(vinylidene fluoride) homopolymer Langmuir–Blodgett nanofilms. *J. Mater. Chem. C* **2**, 6727-6731 (2014).
96. A. J. Lovinger, Polymorphic transformations in ferroelectric copolymers of vinylidene fluoride induced by electron irradiation. *Macromol.* **18**, 910-918 (1985).

국문 초록

원자 재배열을 통한 2차원 물질의 제로 트위스트 구조의 형성

백 지 환

반데르발스(vdW) 층상 구조의 모아레 초격자는 새로운 전자 및 광학 현상을 연구하기 위해 광범위하게 연구되어 왔습니다. 완벽한 제로 트위스트 (zero-twisted) 이중층은 에너지적으로 가장 안정적이지만, 실험적 한계로 인해 적층된 2D 층을 완벽하게 정렬하기는 불가능하고, 자발적인 원자 재구성으로 인해 필연적으로 불균일한 도메인 구조를 형성할 수밖에 없습니다. 본 학위논문에서는 열적으로 유도된 원자 재구성을 통해 뒤틀린 전이금속칼코겐화물 (transition metal dichalcogenide, TMD) 이중층에서의 결맞음 (fully commensurate, FC) 구조의 형성에 대해 연구하였습니다. 이 연구는 결정 방향이 정렬되고 제로 트위스트 TMD 층을 달성하는 새로운 방법을 탐구합니다. 이 연구는 TMD 동종 및 이종 이중층에서 FC 구조의 제작하여 구조의 변화에 따른 광학적, 전기적 특성을 분석하고, 적층 방향에 따른 FC 구조의 원자구조의 제어가 가능함을 연구했습니다. 원자 재구성은 격자 불일치가 큰 이종접합 TMD 이중층에서도 가능하며, in-situ 주사 터널링 전자 현미경(STEM)을 통해 원자 수준의 정렬 메커니즘을 규명합니다. 또한 3R-TMD 이중층의 FC 구조에서 강유전 특성의 향상에 대해 조사했습니다. 본 연구는 TMD 층의 FC 구조 형성에 대한 이해와 새로운 현상 및 응용에 대한 시사점에 기여합니다.